Trends in Physical Chemistry
Vol. 17, 2017

Original Communication

Computational study of chemical shifts in paramagnetic f-element compounds

Helen M. Moylan and Joseph J. W. McDouall*
School of Chemistry, The University of Manchester, Oxford Road, Manchester M13 9PL, UK.

ABSTRACT

The assignment of NMR spectra of paramagnetic species (PNMR) can be a complex undertaking because the presence of unpaired electron spins can cause unpredictable changes in the chemical shifts. The use of quantum chemical methods to assist in the assignment of chemical shifts can potentially provide a valuable tool. Many lanthanide and actinide complexes exhibit open shell electronic configurations and their intricate electronic structures can present severe challenges for quantum chemistry. In this work we report, principally, the proton isotropic shifts for a number of complexes containing a single ion with an f^1 electronic configuration. We also touch on preliminary studies of ^{13}C and ^{29}Si chemical shifts in systems containing an f^3 ion. We employ a methodology based on the computation of spin Hamiltonian parameters and show that it can provide reliable agreement with experimental assignments, and be used to aid the interpretation of experimental PNMR data for f-element compounds. We also show how the formalism can be decomposed to identify and quantify the mechanisms of the paramagnetic effects on the observed spectra, and by doing so offer insight into structure and bonding properties.

KEYWORDS: quantum chemistry, paramagnetic NMR, actinide complexes, proton chemical shifts.

1. Introduction

Experimental and theoretical studies of the lanthanides (Ln) and actinides (An) are of growing interest and importance due to their application in the energy sector, medicine, and advanced technologies [1]. Many of the f-elements have paramagnetic (open-shell) electronic configurations and their consequent magnetic properties make them ideal candidates for research and technology [2]. For example the use of gadolinium contrast agents in Magnetic Resonance Imaging (MRI); neodymium magnets in wind turbines, electric cars and computer hard disks [3]; and lanthanide and actinide single molecule magnets [2]. Understanding the structure, physical and chemical properties of f-element compounds is essential in enabling their exploitation in modern day applications. Various spectroscopic techniques provide key analytical tools for achieving such understanding. In particular nuclear magnetic resonance (NMR) spectroscopy has long been established as a versatile technique that is applied across multiple scientific disciplines including chemistry, physics, biology and medicine [4]. It is a standard technique used for the characterisation of molecules and the investigation of structure and bonding. For diamagnetic (typically closed-shell) molecules assignment of spectra and the extraction of information from their experiments is mostly a routine procedure with the magnitude of the NMR chemical shift easily related to the chemical environment. In addition the development of quantum chemical approaches to predict diamagnetic NMR spectra have been successful and widely applied to aid the analysis and interpretation of experimental data [5-7]. The use of computational predictions is often crucial for the elucidation and identification of complex structures in organic synthesis, natural products chemistry, biochemistry and medicine [8, 9]. However in the

*Email id: joe.mcdouall@manchester.ac.uk

case of paramagnetic f-element ions the application and interpretation of the NMR spectra of f-element compounds is complex.

In paramagnetic molecules, the interaction between the unpaired electron and nuclear spins can cause profound and unpredictable effects, creating NMR spectra that are unrecognisable when compared against a diamagnetic analogue. A simple example to demonstrate this is cyclooctatetraene ($[COT]^{2-}$) which has a ^{1}H NMR shift of 5.8 ppm [10]. The ^{1}H NMR shift of $Th(COT)_2$ (diamagnetic) is 6.2 ppm [10], which is not dissimilar from the free ligand. However in $U(COT)_2$ (paramagnetic) the ^{1}H NMR shift is -36.0 ppm [11]. Paramagnetic NMR (PNMR) shifts can also suffer from line broadening which affects spectral resolution. The intrinsic difficulties associated with the interpretation of PNMR spectra means the full potential of NMR spectroscopy has not been applied to paramagnetic species. This is of particular importance to the lanthanides and actinides due to their role in the nuclear industry. Application of PNMR techniques is required to aid solution speciation of radioactive waste and contamination, and to provide an understanding of the origin of metal-ligand selectivity in waste separation techniques [12-14]. Therefore there is a need to develop computational approaches that reliably predict NMR chemical shifts of paramagnetic species in order to aid the interpretation of experimental data.

Experimentally, the isotropic chemical shift of a paramagnetic molecule is usually described by:

$$\delta_{Exp} = \delta_{Orb} + \delta_{Con} + \delta_{PC} \quad (1)$$

where δ_{Exp} is the observed shift, δ_{Orb} is the orbital shift (analogous to the observed shift in a diamagnetic compound), δ_{Con} is the contact shift and δ_{PC} is the pseudocontact shift. The contact shift originates from the delocalisation of electron spin density from the metal centre to the ligand nuclei, which is mediated by chemical bonding. The pseudocontact shift describes the effects caused by through-space dipolar interactions between the spin of the unpaired electron(s) and the nucleus of interest. This implies that the influence of paramagnetic ions on NMR spectra is determined by the structure and bonding in a system. f-element chemists are interested in the deconvolution of Equation (1) to quantify δ_{Con} and therefore be able to directly compare bonding of the lanthanides and actinides [12-14]. In doing so, they wish to establish a molecular understanding for the metal-ligand selectivity in Ln/An separations which is currently not fully understood [14]. For lanthanide complexes δ_{Con} is often assumed to be negligible due to weak participation of the 4f orbitals in bonding. However, NMR experiments in reference [14] showed that this is not necessarily the case. Hence this is a realm where theoretical calculations should provide valuable insights into the terms that enter Equation (1) and the factors that govern the observed PNMR spectra. An improved understanding of f-element bonding would promote the development of new and improved separation techniques [13].

The difficulties associated with interpreting PNMR spectra span the entire periodic table. The history and development of theoretical approaches to calculate the chemical shift in paramagnetic systems is outlined in reviews by Vaara [15] and Autschbach [16]. The use of quantum chemistry to calculate PNMR spectra of main group and organic radicals has achieved reliable accuracy [17-21]. Extension to transition metals systems has also been successful and has provided useful insight into experimental data [19-33]. However for complexes containing the lanthanides and actinides, accurate prediction of paramagnetic NMR shifts becomes rather more difficult. The complex electronic structure of the f-elements presents severe tests for computational quantum chemistry [34]. The range of electronic effects that must be successfully treated include those of relativity on the ordering of orbital levels, the (near) degeneracies in the valence orbitals and the consequent low-lying excited electronic states. A further key requirement is the adequate treatment of spin-orbit coupling, as this is responsible for coupling electronic states and is key in determining the electronic **g** tensor that enters the computation of PNMR chemical shifts (see 'PNMR theory' section) [35]. In comparison with the rest of the periodic table, there are relatively few examples of calculated PNMR shifts for f-element containing compounds, with most studies focusing on approximate schemes for lanthanide complexes. Autschbach *et al*. [36] studied the paramagnetic NMR shifts in $[Ce(DPA)_3]^{3-}$ using density functional theory (DFT) calculations. They assumed paramagnetic effects to be purely pseudocontact in nature and δ_{Orb} was taken from the diamagnetic

analogue $[La(DPA)_3]^{3-}$. Comparison of the "experimental" and calculated pseudocontact shift for both ^1H and ^{13}C showed reliable agreement. Rodriguez-Rodriguez *et al*. [37] used a similar scheme to calculate ^1H shifts in $[Yb(Me\text{-}DODPA)]^+$. Rodriguez-Rodriguez *et al*. [38] used DFT calculations performed on gadolinium macrocyclic complexes to approximate ^1H shifts in terbium analogues. Fusaro *et al.* [39] employed DFT to successfully aid the interpretation of ^{17}O NMR data from $[Gd(DOTA)]^-$. Gendron *et al*. [40, 41] calculated the ^{13}C NMR shifts for $[UO_2(CO_3)_3]^{5-}$, $[NpO_2(CO_3)_3]^{4-}$ and $[PuO_2(CO_3)_3]^{4-}$ using complete active space self-consistent field (CASSCF) and restricted active space self-consistent field (RASSCF) type calculations. The results obtained were in excellent agreement with experimental data.

In this work our purpose was two-fold. First of all we wished to assess whether we could reliably assign chemical shifts of ^1H, ^{13}C and ^{29}Si nuclei in paramagnetic f-element compounds. Additionally, we investigated whether our computations were able to provide useful insights into the experimental situations and the underlying structure and bonding. Our emphasis was on the ^1H chemical shifts of eight complexes (**1-8**, Figure 1) containing a metal ion (U or Ce) with an f^1 electronic configuration. We adopted a first principles approach in which each term in Equation (1) was assessed to arrive at an adequate computational protocol. A decomposition of the terms in Equation (1) quickly shows that many physical effects enter the theory of PNMR and it is difficult (and in cases unnecessary) to include all of them. (We shall discuss these aspects more fully in the following section.) Our recommended prescription for the computation of PNMR chemical shifts was validated by comparison with reliably assigned experimental spectra. We then extended our study to include ^{13}C and ^{29}Si PNMR chemical shifts and to investigate ions (U or Nd) with an f^3 electronic configuration (**9-14**, Figure 1). We show that our computational approach provides a useful tool in the interpretation, assignment and investigation of paramagnetic f-element compounds by NMR spectroscopy. We conclude by discussing some of the essential extensions to our approach that will increase the reliability and utility of PNMR computations of heavy element compounds.

2. PNMR theory

For the calculation of NMR shifts of paramagnetic molecules we have used the formalism described by Hrobárik *et al.* [22]. The isotropic nuclear shielding, σ_K^{iso}, for a nucleus K, with spin, S, at a temperature, T, is given by

$$\sigma_K^{\mathrm{iso}} = \sigma_{\mathrm{orb}}^{\mathrm{iso}} - \frac{S(S+1)\mu_{\mathrm{B}}}{3k_{\mathrm{B}}Tg_K\mu_{\mathrm{N}}}\left[g_{\mathrm{e}}A_{\mathrm{FC}} + \Delta g_{\mathrm{iso}}A_{\mathrm{FC}} + \tfrac{1}{3}\mathrm{Tr}\left(\Delta\tilde{\mathbf{g}}\cdot\mathbf{A}_{\mathrm{SD}}\right)\right] \tag{2}$$

In Equation (2) the physical constants μ_{B}, μ_{N}, k_{B} and g_K are the Bohr magneton, nuclear magneton, Boltzmann's constant and the nuclear g factor for the nucleus K, respectively. $\sigma_{\mathrm{orb}}^{\mathrm{iso}}$ is the orbital contribution to the chemical shielding (analogous to the chemical shielding in diamagnetic compounds). A_{FC} and $\mathbf{A}_{\mathrm{SD}}$ are the isotropic Fermi contact and anisotropic spin-dipole components of the hyperfine coupling tensor. g_e is the free electron g value, while Δg_{iso} and $\Delta\tilde{\mathbf{g}}$ are components of the $\mathbf{g}$ tensor defined as

$$\Delta\mathbf{g} = \mathbf{g} - g_{\mathrm{e}}\mathbf{I}_3 \tag{3}$$

$$\Delta g_{\mathrm{iso}} = \tfrac{1}{3}\mathrm{Tr}\left[\mathbf{g}\right] - g_{\mathrm{e}} \tag{4}$$

$$\Delta\tilde{\mathbf{g}} = \Delta\mathbf{g} - \Delta g_{\mathrm{iso}}\mathbf{I}_3 \tag{5}$$

There are two terms that we have omitted from Equation (2). The first is the EPR pseudocontact term, A_{PC}, which describes the isotropic spin-orbit contribution to the hyperfine tensor. For light elements we would expect spin-orbit effects to be very small and we have confirmed this through test calculations. We have found that the effect of including A_{PC} on σ_K^{iso} is negligible (whilst being computationally expensive, since it requires the solution of a set of coupled-perturbed orbital equations). Hence A_{PC} has been omitted in our current calculations. More critically, we have also omitted consideration of the effects of Zero Field Splitting (ZFS) on σ_K^{iso}. For systems with more than a single high-spin electron ($S \geq 1$), the coupling of the unpaired spins leads to a splitting of energy levels, even in the absence of a magnetic field. The theory of the role of ZFS in chemical shifts

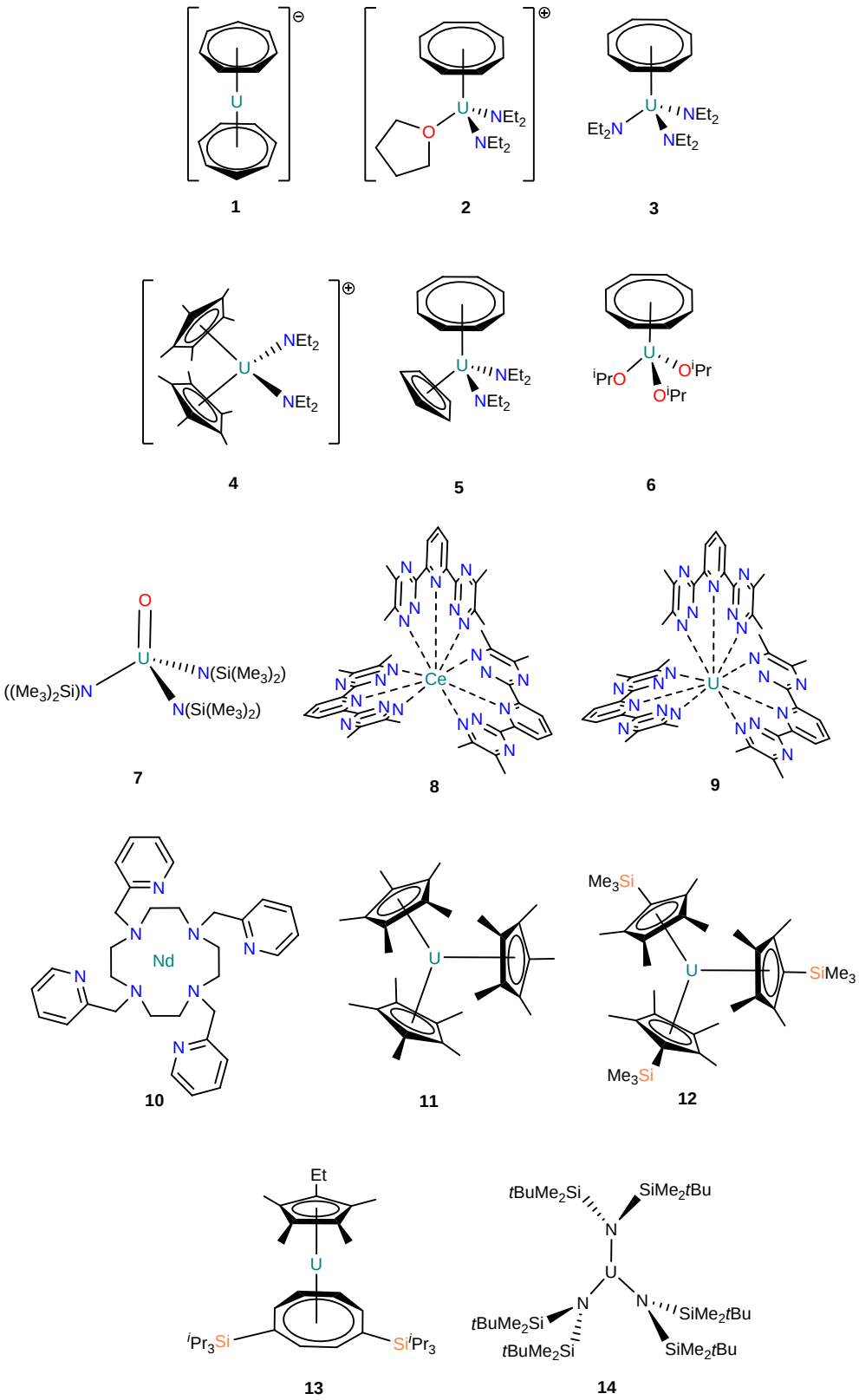

Figure 1. Molecules **1**-**14** are the subject of this work.

has been derived by Soncini and Van den Heuvel [42], and the magnitude of the effects in transition metal complexes has been discussed by Vaara *et al.* [43]. In reference [43] it is shown that ZFS can have a very significant effect on calculated chemical shifts. We shall return to a qualitative discussion of ZFS later, when we consider cases for which $S \geq 1$, but first we shall discuss σ_K^{iso} for the molecules in our dataset that contain ions with f^1 orbital configurations.

For comparison with experiment, the isotropic chemical shift, δ_K^{iso}, is given by:

$$\delta_K^{\mathrm{iso}} = \sigma_{K,\mathrm{Ref}}^{\mathrm{iso}} - \sigma_K^{\mathrm{iso}} \quad (6)$$

where $\sigma_{K,\mathrm{Ref}}^{\mathrm{iso}}$ represents the nuclear shielding of nucleus K in the molecule used as the reference compound for the experimental NMR spectrum. δ_K^{iso} can then be directly compared with δ_{Exp}. From Equation (2) we note that computations of parameters associated conventionally with both NMR (**σ**) and EPR (**g** and **A** tensors) are required to calculate a PNMR chemical shift. Each of these parameters is highly sensitive to their chemical environment and geometry (**R**). Therefore it is essential that accurate crystal structure data, or reliable geometry optimisations, are used to compute each of the component properties. Optimised geometries must be used when considering ^{1}H PNMR chemical shifts. To apply Equation (2) we have four types of calculation to perform, *i.e.* those yielding **R**, **σ**, **A** and **g**. For the lanthanides and actinides these are not routine calculations and therefore the approach for each must be assessed. The methodologies for calculating **R**, **σ**, **A** and **g** are presented and validated in the next section and then used to obtain PNMR chemical shifts in compounds **1-14**.

3. Computational methods

3.1. Geometry optimisations, R

Any electronic structure method used for studying f-element compounds must include the effects of relativity to some extent. Typically, for the geometry, we need only consider scalar relativistic effects. In this study we have used an all-electron approach based on the zeroth order regular approximation (ZORA), as outlined in our previous work [35]. We have written a program, interfaced to the Gaussian [44] quantum chemistry package, in which the ZORA correction to the one-electron Hamiltonian is applied in atomic blocks. This avoids gauge invariance issues and allows the use of codes available for non-relativistic analytical gradients for geometry optimisation, as discussed by van Lenthe [45]. In evaluating the ZORA correction to the kinetic energy we use Filatov's [46] resolution of the identity scheme, which allows the relativistic correction to be obtained using analytic integrals that are readily available in Gaussian. We refer to this scheme as "aZORA". It is simple and efficient to apply and requires minimal extra computational expense over a non-relativistic calculation. Given the types of molecules studied in this work (one Ln/An ion with C/H/N/O/Si-based ligands) the additional basis functions required to perform an aZORA calculation over the use of effective core potentials (ECP) is small, since only the heavy atom would usually be treated with an ECP.

To perform the geometry optimisation step the Segmented All-electron Relativistically Contracted [47, 48] (SARC) basis set was used on the heavy element contracted for the ZORA scheme, and Def2-SVP [49] was used on the light atoms alongside the PBE0 [50] exchange-correlation functional. We expected that DFT would provide a good estimate of geometries, since these are largely determined by the ground state electronic structure. Figure 2 shows the correlation between the aZORA optimised structures and crystal structure data for key bond lengths and angles, from all the molecules we have studied in this work (see Figures 1 and 3 and also Tables S1.1 and S1.2). We see reliable agreement between the observed and calculated geometries, validating this approach. The correlation coefficients obtained for the plots shown in Figure 2 are $R^2 = 1.00$ (bond lengths) and $R^2 = 0.99$ (bond angles).

3.2. Orbital shielding, $\sigma_{\mathrm{orb}}^{\mathrm{iso}}$

$\sigma_{\mathrm{orb}}^{\mathrm{iso}}$ describes the orbital shielding and is analogous to the overall chemical shift in diamagnetic systems. For a diamagnetic molecule, $\sigma_{\mathrm{orb}}^{\mathrm{iso}}$, is observed directly from the recorded NMR spectra. For a paramagnetic molecule we can only observe σ_K^{iso} from NMR

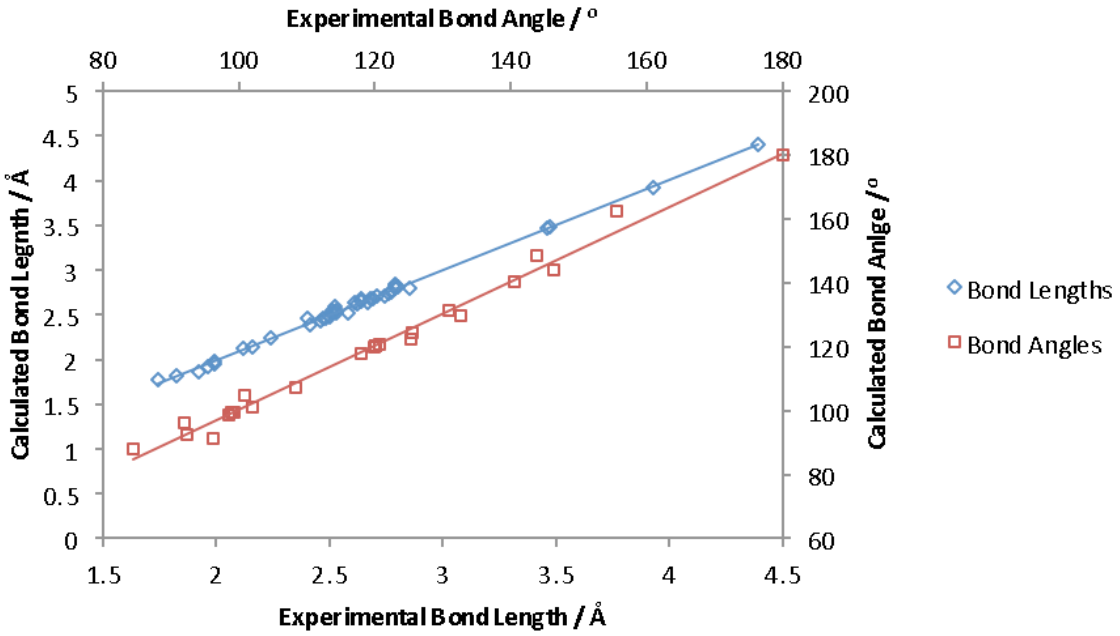

Figure 2. Correlation between optimised geometries and crystal structure data. Key bond lengths and angles are compared. Further details are given in the 'Supporting Information' (S1).

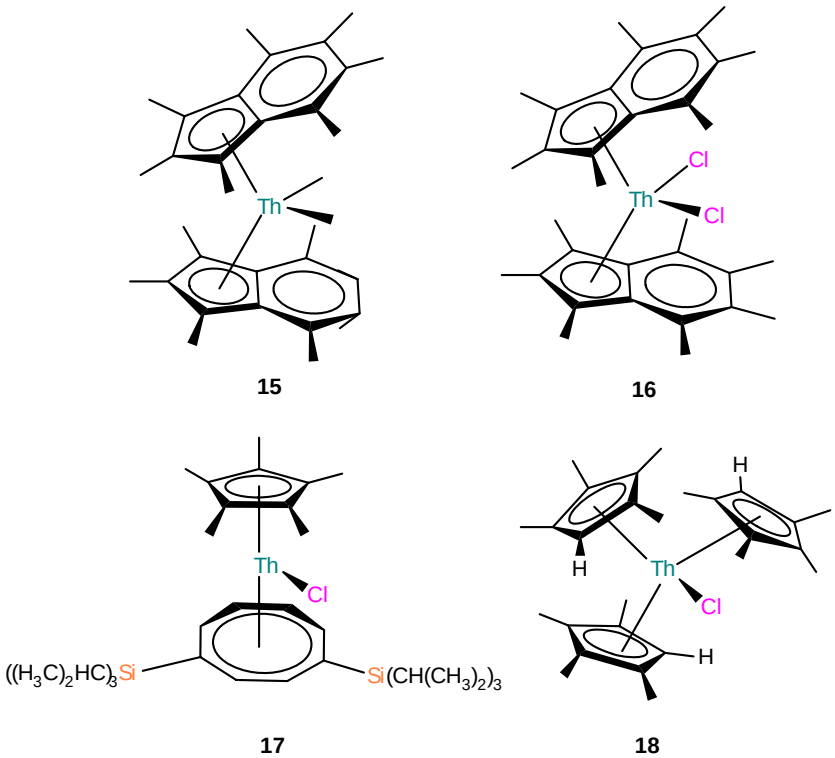

Figure 3. Diamagnetic Th(IV) complexes used in the calibration study of the NMR shielding of heavy element compounds. **15** [Ind*$_2$ThMe$_2$] [51], **16** [Ind*$_2$ThCl$_2$] [51], **17** [Th(COT^{TIPS2})Cp*Cl] [52], **18** [ThCl(η-C$_5$Me$_4$H)$_3$] [53].

experiments (Equation 2). Therefore there is no direct experimental observable of σ_{orb}^{iso} for a paramagnetic molecule. In order to validate our computational approach for this term in f-element compounds, we computed ^{1}H and ^{13}C NMR shifts for a series of diamagnetic Th(IV) compounds [51-53], **15-18**, as shown in Figure 3.

σ_{orb}^{iso} was obtained using gauge including atomic orbitals (GIAO) [54, 55] as implemented in Gaussian [44]. DFT linear response theory (PBE0, SARC basis set on thorium) was used with the aZORA approach to provide a relativistic treatment. Proton chemical shifts were calculated using Def2-TZVP basis on H, and Def2-SVP on all other light nuclei. Carbon shifts were calculated using an uncontracted Def2-SVP basis on C and the regular contracted Def2-SVP on all other nuclei. The results obtained are shown in Figures 4 and 5 for ^{1}H and ^{13}C, respectively. The correlation coefficients for the plots are $R^2 = 0.99$ in Figure 4 and $R^2 = 0.98$ in Figure 5. The correlation shows excellent agreement with the experimental data, which gives confidence in the level of theory used to obtain this term. One clear outlier, however, can be seen in Figure 5. This data point corresponds to the carbon atoms directly bonded to thorium (molecule **15** in Figure 3). Relativistic effects influence the chemical shift of heavy elements significantly but have little effect on light nuclei. However light nuclei that are directly bound to a heavy atom are subject to influences from the heavy element through bonding interactions. These are the so-called heavy atom-light atom (HALA) effects which we observe in our calculations on **15**. For situations where HALA effects are important a more robust theoretical treatment should be sought [56]. For the relatively light nuclei whose shifts have been studied here, given that they are located on ligands and not directly bound to the heavy element, we do not expect such effects to be significant.

In later sections when σ_{orb}^{iso} is computed for use in Equation (2), to calculate the PNMR chemical shift of molecules **1-14**, the formalism described above has been used (GIAO, PBE0, aZORA). For the heavy element the SARC basis set is used with the Def2-TZVP basis set employed on the nuclei of interest. On other nuclei the smallest basis set used was Def2-SVP, with larger sets used where the calculation allowed.

3.3. Hyperfine coupling constants, A

In the literature of f-element compounds there is a paucity of experimental EPR data. This is particularly the case for hyperfine couplings. We were able to find only one example of an f-element hyperfine coupling constant in the literature that could be used for calibrating our methods. The example we used is the proton hyperfine coupling in

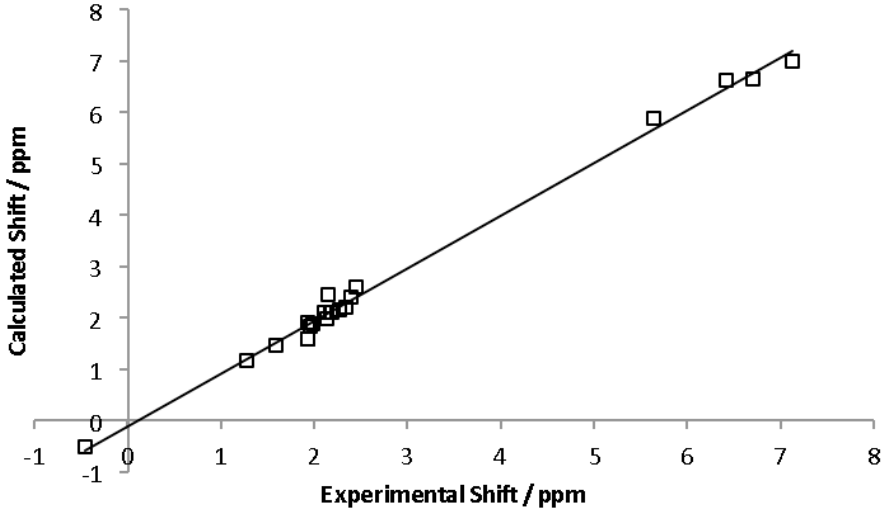

Figure 4. Calculated ^{1}H NMR chemical shifts for **15-18**. See the text for details of basis set and method used.

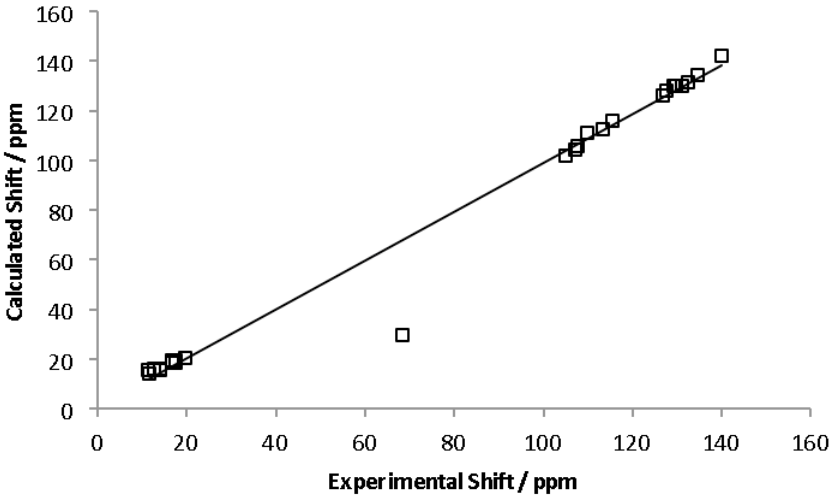

Figure 5. Calculated ^{13}C NMR chemical shifts for **15**-**17**. See the text for details of basis set and method used.

$[U(C_7H_7)_2]^-$ [57, 58] (**1** in Figure 1). To perform computations of the **A** tensor we have used DFT since **A** is a property of the nuclear core and therefore requires correlation of the core electrons. The hyperfine couplings originate from the interaction between an unpaired electron spin and the nuclear spin of a nucleus. The necessary requirements of Gaussian basis sets employed for evaluating hyperfine couplings were enunciated some time ago, *e.g.* see reference [59]. There are a number of basis sets available that have been specifically designed for the calculation of hyperfine couplings (e.g. EPR-II/III [60], IGLO-II/III [61], pcJ-n [62]). Here we have adapted the standard basis sets we use to improve the description of the core region by uncontracting the basis set for the nuclei of interest and including additional steep s-type primitive gaussian functions. The additional steep functions are defined by taking the largest s-type exponents in the basis set of the relevant nuclei and adding extra (uncontracted) functions in geometric progression. Typically 2-3 extra functions showed sufficient convergence in the hyperfine values. Table 1 shows the performance of our modified Def2-TZVP basis set in comparison with the EPR-II/III basis sets for the proton hyperfine couplings in $[U(C_7H_7)_2]^-$. Our modified basis appears to perform similarly to the EPR-III basis set and the approach is easily adapted to any atom of interest.

The proton **A** tensor for $[U(C_7H_7)_2]^-$ was obtained using two types of calculation. In the first method the **A** tensor was produced using the ORCA [63] program (version 3.0.3). Relativistic effects were included using the Douglas-Kroll-Hess transformation to second-order (DKH2) [64, 65]. Picture change transformations [66] of the hyperfine operators were included in these calculations. We refer to this method as $HFCC_1$. In the second method, the **A** tensor was produced using Gaussian with the aZORA scheme but picture change effects were omitted. We refer to this method as $HFCC_2$. Through a number of test calculations we observed that picture change effects for protons were negligible (see Table 2) allowing the use of $HFCC_2$. However for heavier nuclei there was a noticeable effect. The omission of picture change effects caused approximately a 20% and 50% increase in the A_{FC} term for carbon and silicon nuclei, respectively. Therefore for these nuclei we report PNMR shifts calculated using $HFCC_1$ only.

The **A** tensors for molecule **1**, obtained using methods $HFCC_1$ and $HFCC_2$ are shown in Table 2. In each case the PBE0 exchange-correlation functional was used with the SARC basis set on uranium and Def2-TZVP on carbon. We assessed the effects of basis set quality on the proton hyperfine coupling constants by using the following variations of the basis set on hydrogen: (a) Def2-TZVP on hydrogen (b) Def2-TZVP uncontracted on hydrogen with three additional steep functions and (c) Def2-TZVP fully uncontracted on all atoms with three additional steep functions on hydrogen. Both $HFCC_1$ and $HFCC_2$ methods appear to produce similar proton hyperfine coupling constants. Without further

Table 1. Hyperfine couplings for **1** evaluated using EPR-II/III compared with modified Def2-TZVP consisting of an uncontracted H basis with three additional steep s-type functions as described in the text.

Density functional	Basis set	A_{FC}	A^1_{SD}	A^2_{SD}	A^3_{SD}
PBE0	EPR-II	4.7	-1.5	-3.5	4.9
	EPR-III	2.3	-1.6	-3.6	5.1
	Def2-TZVP	2.4	-1.6	-3.5	5.1
B3LYP	EPR-II	1.9	-1.7	-3.3	5.0
	EPR-III	1.9	-1.7	-3.3	5.0
	Def2-TZVP	1.9	-1.7	-3.3	5.0

Table 2. Calculated and experimental A_{FC} and A_{SD} values for **1** given in MHz. All calculations use SARC on uranium and Def2-TZVP on carbon. The carbon and hydrogen basis corresponds to (a) Def2-TZVP (b) Def2-TZVP uncontracted on hydrogen with three additional steep functions and (c) Def2-TZVP fully uncontracted with three additional steep functions on hydrogen.

	A_{FC}	A^1_{SD}	A^2_{SD}	A^3_{SD}
Experimental [58]	-2.7	-2.8	-3.1	+6.0
(a)				
$HFCC_1$	2.3	-1.6	-3.5	+5.1
$HFCC_2$	1.8	-1.7	-3.3	+5.0
(b)				
$HFCC_1$	2.4	-1.6	-3.5	+5.1
$HFCC_1$ (no picture change)	2.5	-1.6	-3.5	+5.1
$HFCC_2$	1.9	-1.7	-3.3	+5.0
(c)				
$HFCC_1$	2.4	-1.6	-3.5	+5.1
$HFCC_2$	2.1	-1.7	-3.4	+5.1

experimental data for comparison it is difficult to comment more on the reliability of each approach. From our experience during this work we found that the **A** tensor calculations using the two different methods always predict a similar pattern in the hyperfine values, which translates to similar patterns in the PNMR shifts generated. Neither method consistently gives better agreement with the experimental data. Hence where applicable (^{1}H) we report PNMR shifts using both methods for comparison and discussion. For assignment and prediction purposes, we found that both methods typically lead to the same conclusion.

The flexibility of the basis set has an effect on the hyperfine coupling constants, in particular for the A_{FC} term, but the effect is not large implying that all the basis sets we employed were of suitable quality for this purpose. This is important since the use of a fully uncontracted basis set is not feasible in general. Overall the basis set effect was more pronounced for the $HFCC_2$ method than for $HFCC_1$. Finally we note that the experimental A_{FC}

value is reported as negative, and our calculated value is positive. However, it is difficult to determine the sign of the hyperfine coupling constants from the experiments in reference [58] and therefore we offer further discussion on this observation later in the text.

For the calculated PNMR chemical shifts of molecules **1**-**14** presented in this work, the basis set used for the **A** tensor is dependent on the nuclei of interest and the size of the molecule. In all calculations Def2-TZVP with three additional steep s-type functions was employed on the nuclei of interest with SARC on the heavy element. The other light nuclei were treated with Def2-SVP or Def2-TZVP depending on the size of the molecule. The exchange-correlation functional, PBE0, was used in all **A** tensor calculations.

3.4. Electronic g tensor

Our recent work on the computation of the Zeeman coupling matrix ("electronic **g** tensor") of U(V) systems [35] discussed issues related to the use of DFT on f-element systems, and favoured the use of State Averaged Complete Active Space Self Consistent Field (SA-CASSCF) calculations to compute this property. Hence SA-CASSCF calculations are the method we have used for the **g** tensor in this work. The SA-CASSCF wavefunctions provide a basis of spin-free states over which the spin-orbit operator is assembled. The evaluation of the **g** tensor can then proceed by forming an effective Hamiltonian, which accounts for the spin-orbit and Zeeman interactions to second order. Comparison of the effective Hamiltonian matrix elements with those of the phenomenological spin Hamiltonian enables the elements of **g** to be identified. This is the approach taken for obtaining **g** in this work and some of the theoretical details can be found in the review by Atanasov *et al.* [67].

All calculations were carried out using the ORCA program [63] (version 3.0.3), with DKH2 treatment of the relativistic effects. Spin-orbit coupling was included using the spin-orbit mean field operator (SOMF(1X)) [68]. The electronic **g** tensor is dependent on the gauge origin used to define the vector potential. Luzanov *et al.* [69] have shown that the gauge dependence can be minimised by choosing the gauge origin as the centre of electronic charge. All calculations reported here use the centre of electronic charge as the gauge origin. For computational efficiency, density fitting approximations were used to calculate the spin-orbit integrals and also for the CASSCF integral transformation. Again the SARC basis set (contracted for the DKH scheme) was used to describe the heavy element. For molecules **1**-**6**, the **g** tensors were obtained using the Def2-TZVP basis set on all light nuclei, in line with reference [35]. All other molecules in this study employed the Def2-SVP basis set on hydrogen and Def2-TZVP on the remaining light nuclei. The active space used for each molecule is tabulated in the Supplementary Information (SI), in Table S2.1. For each molecule the **g** tensor was investigated as a function of the number of states included in the state averaging process and was determined by analysing the spread of excited states to avoid the separation of (near) degenerate states and the inclusion of states too high in energy. For f^1 systems only doublet states were included in the spin-orbit treatment. For f^3 systems quartet and doublet states were included. The calculated PNMR chemical shifts at varying levels of state averaging are fully detailed for each molecule in the SI (section S2).

The choice of technique for obtaining the **g** tensor (not just the principal values) remains something of an open question. In reference [35] we employed an alternative method that is suitable for systems with an odd number of unpaired spins, which manifest a Kramers' degeneracy. In that approach the spin-orbit interaction is applied to obtain the wavefunctions of the degenerate Kramers' pair. The lifting of the degeneracy through the Zeeman interaction is then obtained by rotating the Zeeman operator into the basis of the Kramers' pair, and relating the resulting matrix elements to the components of **g** [70]. For f^1 systems the *g* values obtained by this method and the effective Hamiltonian approach mentioned above are very similar. For f^3 systems we observed that the *g* values obtained from the effective Hamiltonian method and that based on the splitting of the Kramers' degeneracy can be quite different. For example, $[U\{N(SiMe_2tBu)_2\}_3]$ (**14** in Figure 1) has an f^3 configuration with reported experimental *g* values of 0.55, 2.97 and 3.55 [71]. Using the effective Hamiltonian method we obtain computed *g* values of 0.60, 1.74 and 1.74. The calculation incorrectly predicts an apparently axial system

where two of the *g* values are highly underestimated. In contrast the method based on the energy splitting of the Kramers' pair gives *g* values of 0.70, 3.04 and 3.42, which are in much better agreement with the experimental data. Given this, some caution must be exercised when using the effective Hamiltonian method on f^3 molecules. However the recommendation of which method is superior is not so simply resolved as we have found that the elements of **g** obtained by the energy splitting method are much more sensitive to the level of state averaging and can consequently lead to erratic values of σ_K^{iso}. As discussed by Bolvin [70], the **g** matrix obtained by back rotation of the positive square roots of the eigenvalues of $\mathbf{G} = \mathbf{g}\mathbf{g}^{\mathbf{T}}$ can be done in many equivalent ways, without affecting the principal *g* values. At least eight, different, **g** matrices can be defined by this process, with each corresponding to a different choice of phase for the principal *g* values before back rotation to obtain **g**. In fact the signs of the *g* values are not directly determinable, but the sign of the product $g_1g_2g_3$ can be obtained from the magnetic moments $\mu_i(i = 1,2,3)$ that can be evaluated through electronic structure computations [72]. In the ORCA program the **g** tensor is computed by both methods simultaneously, and hence we have been able to compare case by case and we have used the effective Hamiltonian method to obtain **g** throughout this work.

4. Results and discussion

All calculations were performed in the gas phase and compared against experimental NMR data obtained in solution. Clearly, environmental conditions can have an influence on the observed NMR spectra and hence the omission of these effects should be borne in mind. For example, in some cases the experimental spectra exhibit a single broad peak, implying a single chemical environment. This can be at odds with what can be gleaned from consideration of a static molecular structure, as used in our calculations. The PNMR shifts were all calculated relative to tetramethylsilane (TMS). $\sigma_{K,\mathrm{Ref}}^{\mathrm{iso}}$ was calculated using the same basis set and method as $\sigma_{\mathrm{orb}}^{\mathrm{iso}}$. The temperature used in evaluating Equation (2) was taken from the experimental data, where this was indicated, or assumed to be 298 K. In addition many of the experiments describe broad peaks, which should be borne in mind when comparing experimental and calculated peaks.

Our main focus in the study was on the calculation of $\delta_{\mathrm{H}}^{\mathrm{iso}}$ for f^1 f-element systems. Before presenting our summary of results for $\delta_{\mathrm{H}}^{\mathrm{iso}}$ for molecules **1-8** we illustrate some of the issues that arise in this type of calculation by highlighting some key features for specific molecules. Next we show how a decomposition of the terms that enter Equation (2) can provide insight into f-element structure and bonding. In addition, we note that experimental conditions can have a significant effect on the NMR spectra observed for paramagnetic molecules and hence reliable PNMR calculations can be a vital tool for solution speciation techniques. Finally we present some preliminary investigations of ^{13}C and ^{29}Si chemical shifts in systems containing an f^3 ion.

4.1. Paramagnetic chemical shifts, $\delta_{\mathrm{H}}^{\mathrm{iso}}$, for molecules 1-8

4.1.1. Averaging of proton environments

A challenge in predicting isotropic ^1H PNMR chemical shifts arises due to our calculations being based on a single static geometry. Protons in solution, for example within a methyl group, will rotate to some degree. When rotation of chemical groups is faster than the NMR timescale, an average peak is obtained. In order to investigate the influence of this on our computed chemical shifts, the individual ^1H shifts were averaged over all protons of a chemical group. A tacit assumption in this process is that the rotation of methyl, and similar, groups is completely unhindered since each proton contributes equally to the average shift. This process was used on the CH_2 and CH_3 groups in molecules **2-8**. Figure 6 shows the correlation between the experimental and averaged calculated data. The correlation coefficients obtained are $R^2 = 0.92$ ($HFCC_1$) and $R^2 = 0.91$ ($HFCC_2$). The results suggest that the approximation made is reasonable. A better procedure would be to use a Boltzmann-weighted vibrational average of the chemical shifts to better account for the dynamics of proton-containing groups. However this was not attempted due to the large computational expense that would

be incurred. The averaging of group proton shifts appears to be an appropriate starting point for addressing the issue.

4.1.1.1. $[U(C_7H_7)_2]^-$, 1

The case of $[U(C_7H_7)_2]^-$ provides a useful example as EPR, NMR and crystal data are all available for comparison with our calculations. The ^{1}H NMR spectra exhibit one broad peak at -38.7 ppm [57]. We have already seen that the computed A_{FC} and A_{SD} values from Table 2 show good agreement with the experimental data. The SA-CASSCF calculation (5 electrons in 9 orbitals) with 15 states included, gives *g* values of 1.26 and 2.36 which are in excellent agreement with the experimental data as fully discussed in reference [35]. Table 3 shows the calculated ^{1}H NMR shift of $[U(C_7H_7)_2]^-$ for various levels of state averaging using the two methods, $HFCC_1$ and $HFCC_2$, for the **A** tensor calculation.

The calculations predict a large negative shift in line with the experimental data. Both methods underestimate the shift, with $HFCC_1$ offering better agreement. The A_{FC} values from the $HFCC_1$ method are greater in magnitude than those obtained from $HFCC_2$ (see Table 2), and this is echoed in the total chemical shifts. In the discussion of hyperfine values for **1** (see Table 2 and text) we noted a discrepancy between our calculated values of A_{FC} and that inferred from experiment [58]. Taking the chemical shifts produced by state averaging 31 states in the **g** tensor calculation, we repeated the calculation of Equation (2) with the sign of A_{FC} reversed. This yielded total δ_H^{iso} values of +50.47 ppm ($HFCC_1$) and +41.46 ppm ($HFCC_2$). The sign of δ_H^{iso} is now opposite to that of the experiment and also the magnitude is in poorer agreement. Given this data we favour the view that A_{FC} should be taken as positive.

δ_H^{iso} for **1** was also calculated using the basis set (c) from Table 2. The results are given in Table S2.2 in the SI. As noted earlier, the hyperfine values from $HFCC_2$ have a greater dependence on basis set than $HFCC_1$ and this is transferred to the computed PNMR shifts. By increasing the size of the basis an improvement in $HFCC_2$ results, by approximately 2-3 ppm, is observed with little change in the results from $HFCC_1$.

4.1.1.2. $[(\eta^8\text{-}C_8H_8)U(NEt_2)_2(THF)]^+$, 2

Molecule **2** has multiple proton environments which enabled us to assess the performance of our calculations in predicting the spectral range and the relative position of observed peaks. The experimental ^{1}H spectrum for **2** shows three resonances at 31.2 ppm, 3.8 ppm and -15.3 ppm assigned as CH_2, CH_3 and C_8H_8, respectively [73]. Tables 4 ($HFCC_1$) and 5 ($HFCC_2$) show our results as a function of the level of state averaging. The calculated results agree with the experimental assignment, predicting one large positive shift (CH_2),

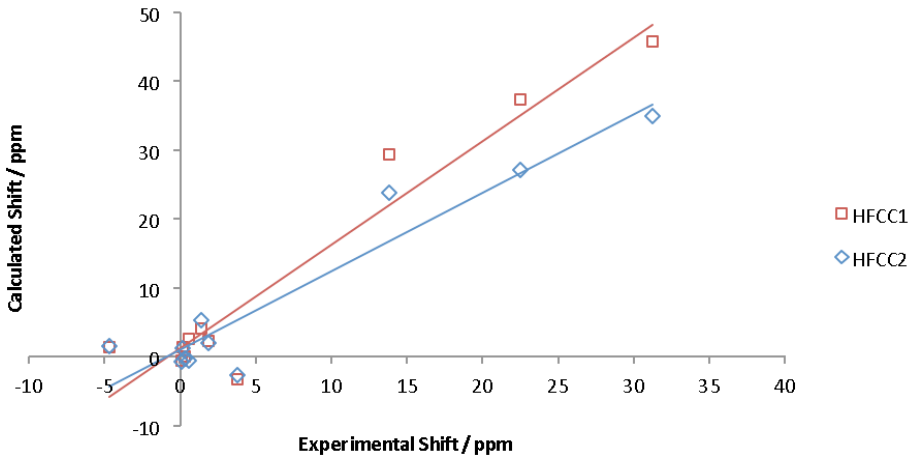

Figure 6. Correlation between experimental and group averaged calculated ^{1}H shifts for molecules **2-8** from groups that have been averaged.

Table 3. Calculated isotropic ^{1}H PNMR shifts for **1** as a function of the number of states included in the SA-CASSCF **g** tensor calculation. The hyperfine calculations were taken from (b) in Table 2. Specification of basis sets and methods used to calculate each component of Equation (2) can be found in the 'Computational methods' section. δ_H^{iso} is given in ppm.

Number of states averaged (g tensor)	**($HFCC_1$ / A tensor)**	δ_H^{iso}	**($HFCC_2$ / A tensor)**
Experimental [57]	*-38.7*		
5	-29.4		-20.3
7	-29.4		-20.3
9	-29.6		-20.5
11	-28.8		-19.8
15	-29.2		-20.1
21	-34.7		-24.3
31	-35.1		-24.6
41	-33.8		-23.6
61	-34.0		-23.7
101	-32.9		-22.9

one large negative shift (C_8H_8), and a small shift from the reference molecule (CH_3). As we have noted previously, the level of state averaging can have a large effect on the *g* values obtained [35]. However for the PNMR shift, the number of states included appears to affect only the magnitude of the chemical shift, and the assignment and ordering of peaks does not change. In the case of **2**, including more states only serves to increase the size of the calculated shifts. This is evident in other cases as shown in Table 3 and section S2 in the SI. Similarly with molecule **1**, the calculation of the **A** tensor using the $HFCC_1$ method gives larger A_{FC} values ($HFCC_1$/MHz: -3.77, 0.089, 2.53 and $HFCC_2$/MHz: -2.81, 0.066, 2.15 for CH_2, CH_3 and C_8H_8, respectively) and this again is transferred into larger PNMR shifts. However, for molecule **2**, $HFCC_2$ gives better agreement with the magnitudes of the experimental shifts. This is in contrast to our results for molecule **1**. As mentioned earlier, there is no consistently superior choice between the use of $HFCC_1$ and $HFCC_2$ and the results for molecules **1** and **2** are evidence for this. It is therefore useful to report the results based on both methods.

4.1.1.3. $[(\eta^5\text{-}C_5Me_5)_2U(NEt_2)_2]^+$, 4

The experimental spectrum of **4** exhibits broad peaks so that the assignment of each of the individiual proton environments was not possible [74]. A broad resonance at 14.1 ppm is assigned to a combination of the $C_5(CH_3)_5$ and CH_2 groups, and a broad resonance at -4.7 ppm corresponds to the CH_3 groups. To compare with the experimental shifts, we averaged the $C_5(CH_3)_5$ and CH_2 groups. The calculated values in comparison with the experimental assignments are shown in Table 6.

The $HFCC_2$ results show good agreement with the experiment and are able to reproduce the relative shift between the two assigned peaks (18.8 ppm v 17.1 ppm). Due to the difficulties in assigning the experimental spectrum we can use our calculations to provide further insight into the interpretation of the data. From the crystal structure (or the optimised structure), it can be observed that each of the carbon atoms of the methyl groups on Cp* are not in equivalent environments. The U-C distances (red arrows as shown in Figure 7) range from 3.79 to 3.98 Å in the crystal structure (3.72 to 3.92 Å in the optimised structure).

Similarly, each of the CH_2 groups from the ethyl pendants are not equivalent, the U-C distances in this case (green arrows as shown in Figure 7) range from 2.92 to 3.45 Å in the crystal structure (2.92 to 3.37 Å in the optimised structure). We would anticipate that the torsion of the NEt_2

Table 4. Calculated isotropic ^{1}H PNMR shifts for **2** using the $HFCC_1$ method for the **A** tensor. The number of states averaged in the SA-CASSCF **g** tensor calculation is given in the first column. Specification of basis sets and methods used to calculate each component of Equation (2) can be found in the 'Computational methods' section. δ_H^{iso} is given in ppm.

Number of states averaged (g tensor)	δ_H^{iso}		
	(CH_2)	**(CH_3)**	**(C_8H_8)**
Experimental [73]	*31.2*	*3.8*	*-15.3*
4	45.8	-3.2	-22.7
5	49.9	-2.5	-33.0
7	52.6	-2.9	-34.0
8	53.3	-3.1	-35.1
16	56.4	-3.8	-38.6
18	57.0	-3.6	-38.3
20	57.7	-3.5	-38.4
28	58.9	-3.9	-40.0
30	58.9	-4.1	-40.4
31	59.2	-4.1	-40.7
40	59.3	-4.4	-41.7
50	60.2	-4.4	-42.4
90	60.1	-4.5	-42.1

Table 5. Calculated isotropic ^{1}H PNMR shifts for **2** using the $HFCC_2$ method for the **A** tensor. The number of states averaged in the SA-CASSCF **g** tensor calculation is given in the first column. Specification of basis sets and methods used to calculate each component of Equation (2) can be found in the 'Computational methods' section. δ_H^{iso} is given in ppm.

Number of states averaged (g tensor)	δ_H^{iso}		
	(CH_2)	**(CH_3)**	**(C_8H_8)**
Experimental [73]	*31.2*	*3.8*	*-15.3*
4	35.0	-2.6	-18.2
5	36.9	-1.9	-27.3
7	39.0	-2.3	-28.1
8	39.4	-2.5	-29.0
16	41.4	-3.1	-32.0
18	42.0	-2.9	-31.8
20	42.7	-2.8	-31.9
28	43.3	-3.2	-33.2
30	43.3	-3.4	-33.6
31	43.5	-3.4	-33.8
40	43.3	-3.7	-34.7
50	44.0	-3.7	-35.3
90	44.0	-3.7	-35.1

Table 6. Experimental and calculated isotropic ^{1}H PNMR shifts for **4** using $HFCC_1$ and $HFCC_2$ for the **A** tensor calculation. Specification of basis sets and methods used to calculate each component of Equation (2) can be found in the 'Computational methods' section. $\delta_{\mathrm{H}}^{\mathrm{iso}}$ is given in ppm.

	Experiment [74]	$\delta_{\mathrm{H}}^{\mathrm{iso}}$ **($HFCC_1$ for A tensor)**	**($HFCC_2$ for A tensor)**
$C_5(CH_3)_5$ and CH_2	14.1	26.2	18.6
CH_3	-4.7	1.4	1.5
Difference	18.8	24.8	17.1

groups is well represented by the averaging done in our calculations. Equally we would expect the carbon atoms in $C_5(CH_3)_5$ to be relatively static, implying that each of the methyl groups are not equivalent. Table 7 shows the calculated ^{1}H NMR shift of each of the ten methyl groups (**a–j** as shown in Figure 7), which ranges from -6.7 to 27.6 ppm. We reiterate that all calculations were done in the gas phase, and therefore we have not attempted to represent the geometry under the influence of solvent or vibrational averaging. However, this range of peaks for the $C_5(CH_3)_5$ methyl protons could explain the difficulties in assigning the spectrum.

4.2. Summary of $\delta_{\mathrm{H}}^{\mathrm{iso}}$ results for molecules 1-8

The results for all the calculated ^{1}H PNMR shifts for molecules **1-8** are shown in Table 8. All of these systems have f^1 electronic configurations on the metal. Figure 8 shows the correlation between the calculations and experimental data. When comparing the two different methods used for the **A** tensor, we see that $HFCC_1$ (ORCA 3.0.3/DKH2) produces larger shifts compared with $HFCC_2$ (Gaussian/aZORA). The correlation coefficients obtained are R^2 = 0.88 ($HFCC_1$) and R^2 = 0.89 ($HFCC_2$) implying that there is no clear preference for the case of proton chemical shifts. In most cases the calculated shifts are overestimated; however the spectral pattern is identifiable. Since the choice of method used ($HFCC_1$/$HFCC_2$) doesn't affect the relative ordering of shifts, either method can be used for the assignment of ^{1}H PNMR spectra.

4.3. Lanthanide compared with actinide

As discussed in the introduction and shown in Equation (1), paramagnetic effects on the NMR shift of ligand nuclei can be separated into through-bond (contact) and through-space (pseudocontact) interactions. As discussed in reference [22], $g_e A_{\mathrm{FC}}$ and $\Delta g_{\mathrm{iso}} A_{\mathrm{FC}}$ can be associated with the contact shift, and $\Delta\tilde{\mathbf{g}} \cdot \mathbf{A}_{\mathrm{SD}}$ with the pseudocontact shift. Inspection of the individual terms allows us to probe bonding and structural effects. Equation (2) can be written as

$$\sigma_K^{\mathrm{iso}} = \sigma_{\mathrm{orb}}^{\mathrm{iso}} + f g_{\mathrm{e}} A_{\mathrm{FC}} + f \Delta g_{\mathrm{iso}} A_{\mathrm{FC}} + \tfrac{1}{3} f \mathrm{Tr}\left(\Delta\tilde{\mathbf{g}} \cdot \mathbf{A}_{\mathrm{SD}}\right) \tag{7}$$

where

$$f = -\frac{S(S+1)\mu_{\mathrm{B}}}{3k_{\mathrm{B}} T g_K \mu_{\mathrm{N}}} \tag{8}$$

Table 7. Calculated isotropic ^{1}H PNMR shifts from methyl groups of Cp* rings of **4** using $HFCC_2$ to calculate the **A** tensor. Specification of basis sets and methods used to calculate each component of Equation (2) can be found in the 'Computational methods' section. $\delta_{\mathrm{H}}^{\mathrm{iso}}$ is given in ppm.

	$\delta_{\mathrm{H}}^{\mathrm{iso}}$
a	24.5
b	13.7
c	7.8
d	-1.5
e	-6.7
f	27.6
g	0.2
h	14.5
i	7.5
j	15.5
Average CH_3	10.3

We can define the NMR shift in a paramagnetic molecule to be the orbital shielding plus three paramagnetic terms, FC_1, FC_2 and PC.

$$\sigma_K^{iso} = \sigma_{orb}^{iso} + FC_1 + FC_2 + PC \quad (9)$$

We wished to compare the contact and pseudocontact effects for lanthanide and actinide analogues. Using as suitable examples trivalent $[Ce(Mebtp)_3]^{3+}$, **8**, and $[U(Mebtp)_3]^{3+}$, **9** [77, 78], we show the values calculated for FC_1, FC_2 and PC in Table 9. The values calculated for PC give similar results, with low values obtained for both molecules. This can be attributed to both molecules having similar geometric structures. The bond angles between the metal centre and the ligands are the same, but the uranium-Mebtp distances are shorter than for the cerium analogue. Comparing terms FC_1 and FC_2, the values calculated for **9** are up to 150 times larger, which is indicative of the difference in bonding interactions between **8** and **9**. There is currently much interest in the nature of chemical bonding for lanthanides and actinides [12-14, 79-81]. This is an important area in nuclear chemistry research where selective separation of lanthanides and actinides from nuclear waste is required. 4f orbitals are thought to participate weakly in bonding and have "core-like" behaviour. In contrast, 5f orbitals extend further and are perturbed appreciably as they participate in covalent bonding [81]. The values of FC_1 and FC_2 concur with these ideas given the calculated contact shifts are much larger in magnitude for the uranium analogue.

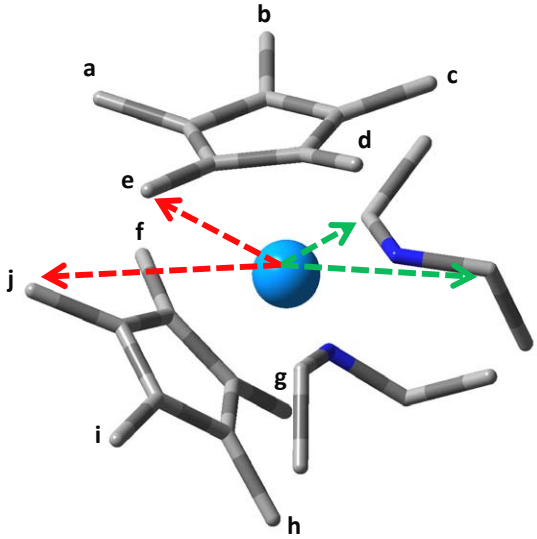

Figure 7. Molecule **4** with methyl groups **a–j** highlighted. Arrows indicate the U-C distances discussed in the text.

A further consideration now is that the U(III) ion in **9** possesses an f^3 orbital consideration and so is subject to the effects of ZFS. The deviation of δ_H^{iso} from the experimental values is quite severe. The largest magnitude shifts are too large in both

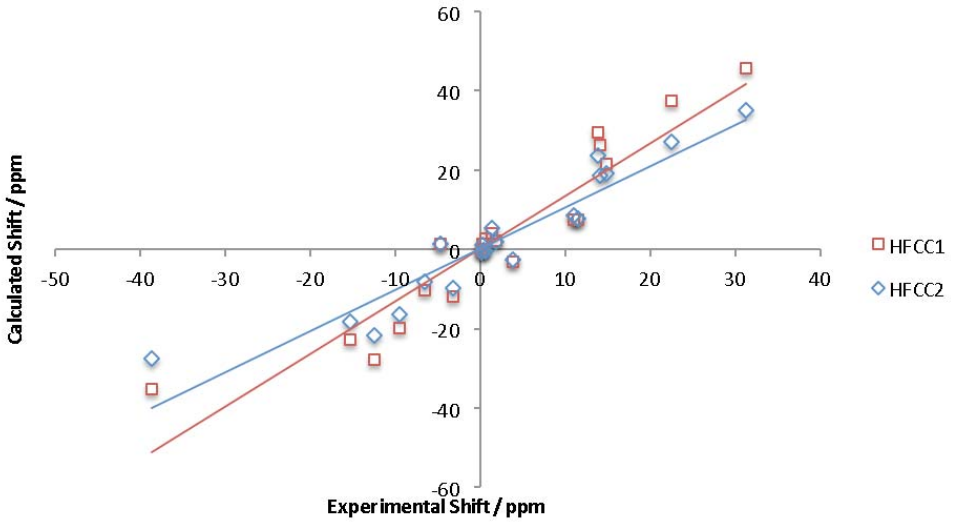

Figure 8. Correlation between calculated and experimental ^{1}H shifts obtained for molecules **1-8**. For data and details of calculations see Table 8.

Table 8. Calculated and experimental ^{1}H PNMR chemical shifts in f^1 systems, **1-8**. δ_H^{iso} is given in ppm. For specification of basis sets and methods used to calculate each component of δ see the 'Computational methods' section. [(a)]Data from two separate sources have been averaged. [(b)]Data from four experiments have been averaged. [(c)]In **8** there are two different methyl groups present and the experiment is unable to distinguish between them. The calculated and experimental chemical shifts have been ordered numerically for comparison.

		Experiment	δ_H^{iso} (HFCC$_1$ for A tensor)	(HFCC$_2$ for A tensor)
1	C_7H_7	-38.7 [57]	-35.1	-27.4
2	CH_2	31.2 [73]	45.8	35.0
	CH_3	3.8 [73]	-3.2	-2.6
	C_8H_8	-15.3 [73]	-22.7	-18.2
3	CH_2	13.8 [73]	29.4	23.8
	CH_3	0.2 [73]	1.4	1.2
	C_8H_8	-9.5 [73]	-19.8	-16.3
4	$C_5(CH_3)_5$ and CH_2	14.1 [74]	26.2	18.6
	CH_3	-4.7 [74]	1.4	1.5
5	C_8H_8	-12.5 [73]	-27.8	-21.7
	CH_3	0.3 [73]	0.1	-0.3
	C_5H_5	-3.2 [73]	-11.9	-9.8
	CH_2	22.5 [73]	37.4	27.1
6	$C\underline{H}Me_2$	14.8 [73]	21.5	19.2
	$CH(C\underline{H}_3)_2$	1.8 [73]	2.3	2.1
	C_8H_8	-6.6 [73]	-10.4	-8.2
7	$SiMe_3$	0.1[(a)] [75,76]	-0.6	-0.7
8	3,5-py	11.5[(b)] [77,78]	7.6	7.7
	4-py	11.0[(b)] [77,78]	7.6	8.6
	CH_3[(c)]	1.4[(b)] [77,78]	4.1	5.3
	CH_3[(c)]	0.6[(b)] [77,78]	2.6	-0.6

directions and the two intermediate values appear in the wrong order. We have made no attempt to include the effects of ZFS rigorously but can call on various schemes, including some extreme approximations, to look qualitatively at the influence of ZFS. References [22] and [27] have provided useful closed form expressions indicating the dependence of the contact (FC_1 + FC_2) and pseudocontact (PC) shifts on ZFS. We find the SA-CASSCF calculations, including 14 quartet and 25 doublet states, used to obtain the **g** tensor, yield an axial zero field splitting constant, D = 21.7 cm^{-1} and principal g values of 0.17, 1.29 and 1.35. Under the assumption of axial symmetry [27], re-evaluating δ_H^{iso} using the D and g values above, changes the largest positive value from 67.5 ppm to 20.2 ppm. For the largest negative value, δ_H^{iso} changes from -48.4 ppm to -25.4 ppm. Both of the outer lying shifts are now closer to the observed values, but applying the same procedure to the two inner values (-23.5 ppm and 21.5 ppm) yields -28.5 ppm and 25.0 ppm, which show relatively little change and are actually in poorer agreement with the observed values. This simple exercise highlights the importance of ZFS and

Table 9. Comparison of calculated FC_1, FC_2 and PC terms in Equation 9 and δ_H^{iso} (all quantities in ppm) for the four proton environments in molecules **8** and **9**. $HFCC_1$ was used for the **A** tensor calculation. Specification of basis sets and methods used to calculate each component of Equation (2) can be found in the 'Computational methods' section. For **9** the **g** tensor calculation includes 14 quartet and 25 doublet states. [(a)]For **8** the experimental value is an average from four experiments and for **9** the experimental value is an average of two experiments, as reported in references [73] and [74]. [(b)]In **8** and **9** there are two different methyl groups present and the experiment is unable to distinguish between them. The calculated and experimental chemical shifts have been ordered numerically for comparison.

	FC_1	FC_2	PC	δ_H^{iso}	
				This work	**Experiment[(a)]**
$[Ce(Mebtp)_3]^{3+}$, **8**					
4-py	1.1	-1.7	3.4	7.6	11.0
3,5-py	0.3	-0.5	3.8	7.6	11.5
CH_3[(b)]	0.5	-1.0	-2.6	4.1	1.4
CH_3[(b)]	-1.1	1.8	-0.9	2.6	0.6
$[U(Mebtp)_3]^{3+}$, **9**					
4-py	155.9	-228.8	14.5	67.5	33.1
3,5-py	-49.7	73.0	10.0	-23.5	6.0
CH_3[(b)]	28.8	-42.3	-6.3	21.5	4.6
CH_3[(b)]	-113.4	166.6	-2.1	-48.4	-17.5

also illustrates the need to incorporate it into the calculations rigorously. It should not be assumed that all shifts will be affected significantly by ZFS, see the examples in reference [43], but given the effects can be very substantial its inclusion is essential for even semi-quantitative studies.

4.4. Structural and environmental effects

Chemical shifts are highly dependent on geometric structure and environmental influences. We investigated the effects of solvent and counter ions on the geometry and chemical shifts calculated for a neodymium analogue of a tetrapyridyl appended cyclen ($[Nd.L^{py}]^{3+}$) [82], as shown in Figure 9 (and molecule **10** in Figure 1). We found that the inclusion of solvent, through a polarisable continuum model [83-85], had a negligible effect on the optimised geometry. However the inclusion of a triflate anion in the cavity (as seen in the crystal structure) has pronounced effects on the geometry of **10** that contains an f^3 metal ion and so is subject to the effects of ZFS. In addition, the experimental spectrum only identifies nine peaks whilst there are ten proton environments. Hence, rather than directly comparing values of δ_H^{iso} we investigated the spectral range corresponding to chemical shifts without (geometry 1, Figure 9a) and with (geometry 2 Figure 9b) the triflate anion in order to analyse the structural implications. The experimental chemical shifts range from 12.4 ppm to -0.2 ppm. Our calculations (using $HFCC_1$ for the **A** tensor calculation and 21 quartet states and 40 doublet states included in the SA-CASSCF **g** tensor calculation) produced a range of 27.4 ppm to -14.0 ppm for geometry 1. For geometry 2, the range was 16.5 ppm to -2.6 ppm. The presence of the triflate group gives better agreement with the experimental data predicting a much smaller range of chemical shifts.

Accordingly we propose that the probable solution structure of **10** contains the triflate ion coordinated to neodymium. The coordination of the triflate counterion to the metal centre is not a passive effect and must be included when modelling this structure. These results emphasise that an understanding of the experimental conditions is required when comparing PNMR calculations with experimental data. PNMR

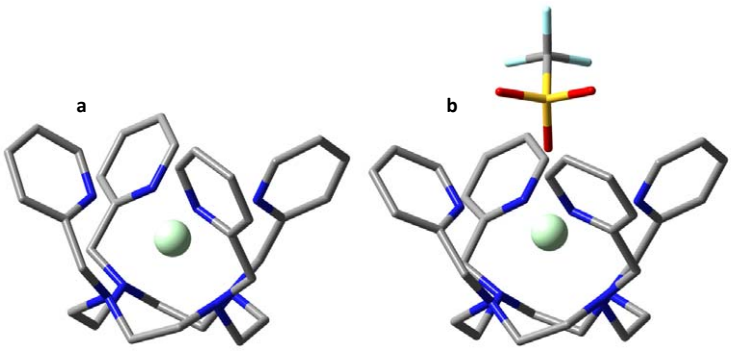

Figure 9. Optimised geometries (a) without and (b) with the triflate anion for molecule **10** (PBE0, aZORA, SARC basis set on Nd and Def2-SVP basis set on all other nuclei).

Table 10. Calculated ^{1}H and ^{13}C PNMR chemical shifts in **11** using $HFCC_1$ at the optimised geometry. δ^{iso} values in ppm. Specification of basis sets and methods used to calculate each component of Equation (2) can be found in the 'Computational methods' section.

Experiment [86]		δ_H^{iso}	δ_C^{iso} **(Cp ring)**	δ_C^{iso} **(Me)**
		-0.9	*324.8*	*-86.7*
Number of states averaged (g tensor)				
Quartets	**Doublets**			
6		-1.7	131.4	-68.9
12		-0.3	177.9	-66.8
12	3	0.7	159.3	-34.0
14		1.6	173.4	-8.7
14	8	0.8	193.0	-52.7
19		-1.6	170.1	-91.9
20		0.5	123.2	-11.4
20	23	1.0	197.9	-45.6
27		-2.6	121.8	-85.8
28		-2.6	124.1	-86.3
28	55	-3.0	132.0	-102.2
30		-2.6	121.8	-84.2
35		-2.7	127.3	-90.6

spectra are extremely sensitive to structure, environment, charge and oxidation state. Hence reliable prediction of PNMR spectra can offer a route to improving characterisation methods for f-element compounds and understanding solution speciation.

4.5. δ_H^{iso} and δ_C^{iso} for molecule 11

Keeping in mind the previous caveats associated with the role of ZFS in f^3 systems we have studied the ^{1}H and ^{13}C PNMR chemical shifts in **11**. It provides a useful illustration of the effect of the inclusion of excited states in the state averaging process and the need to test the level of state averaging for each individual case. Table 10 shows δ_H^{iso} and δ_C^{iso} obtained using the optimised geometry of **11** with the $HFCC_1$ approximation for the **A** tensor.

The δ^{iso} values stabilise after the inclusion of around 27 excited quartet states. The inclusion of doublet states into the state averaging process (and the subsequent evaluation of the **g** tensor) produces an increase in the magnitude of all three shifts in **11**. The negative δ^{iso} values are in error by approximately

Table 11. Calculated ^{29}Si PNMR chemical shifts in **12**, **13** and **14** ($HFCC_1$ for the **A** tensor). δ^{iso} values in ppm. Specification of basis sets and methods used to calculate each component of Equation (2) can be found in the 'Computational methods' section. [(a)]Crystal geometry used. [(b)]Optimised geometry used. [(c)]Number of states included in the state averaging procedure.

	δ_{Si}^{iso}			
	12[(a)]	**13**[(a)]	**14**[(a)]	**14**[(b)]
Experiment	-155.0 [87, 88]	-136.7 [89]	-296.0 [71]	
	-136.1	-174.3	-374.7	-314.6
No. Quartets[(c)]	21	13	21	21
No. Doublets[(c)]	39	32	39	39

2 ppm and 16 ppm. For the large positive δ^{iso} value the error is 193 ppm! These discrepancies might be attributable to the influence of ZFS, although it is difficult to be certain without a proper calculation of that effect. However in this case we are able to assign observed chemical shifts from our calculations, as the pattern of shifts is reproduced very well. So even in the absence of a complete theoretical treatment, these calculations are able to offer insight and utility.

4.6. δ_{Si}^{iso} for molecules 12, 13 and 14

We also investigated δ_{Si}^{iso} for molecules **12**, **13** and **14** and our results are shown in Table 11. Given the large shift values we report the level of state averaging that produced results stable to ± 5 ppm. Although the absolute values are in error by as much as 79 ppm, these large shifts are predicted with a reasonable, order of magnitude, accuracy. We also note from these results that the values obtained can be very sensitive to the geometry used. Where possible it is advisable to test both crystal geometries and those obtained through optimisation.

5. Conclusions

The computation of NMR shifts in paramagnetic molecules, using a formalism related to spin Hamiltonian parameters, depends critically on four computed quantities: (i) molecular geometry, (ii) the orbital chemical shielding, (iii) the hyperfine tensor and (iv) the electronic **g** tensor. As we have illustrated here (and in reference [35]) each of these terms can require different levels of theoretical and computational treatment to obtain reliable estimates. This is particularly the case in f-element compounds, which have been the focus of interest in this work. The lanthanides and actinides have complex electronic structures, subject to strong relativistic effects. Apart from relativistic effects there is a need to treat dynamic and non-dynamic electron correlation adequately. Both ground states and excited states must, in principle, be considered for states of $\Delta S = 0, \pm 1$ relative to the ground spin state. We have considered each of these required components and provided preliminary recommendations for the computational level necessary. Applying these methods, we have demonstrated useful agreement between calculation and experiment. In particular this is true for f^1 electronic configurations. In these cases, the pattern in shifts is identifiable and comparable with experimental assignments, giving confidence that these computations can be used to aid the interpretation of PNMR spectra of such compounds.

When considering ions with f^3 electronic configurations the situation is less robust. The quality of results obtained shows much more variation and the absolute magnitudes of PNMR shifts are less well reproduced. The omission of ZFS effects in the calculations is almost certainly a major contributor to this and its inclusion in any further studies of systems for which $S \geq 1$ is essential. Other aspects of the electronic structure methods used that should be improved must include a better treatment of the dynamic electron correlation problem when evaluating **g** tensors. This can be achieved reasonably economically by using perturbation theory (*e.g.* NEVPT2 [90-92]) to provide improved energies of the spin free states that enter the spin-orbit coupling problem. However, ultimately, a higher order treatment of the spin-orbit coupling is likely to be necessary for dealing reliably with heavy element systems.

Using a PNMR formalism (Equation 2) that is based on spin Hamiltonian parameters (**A**, **g**) makes the

assessment of computational protocols for these terms somewhat difficult as there is a dearth of reliable experimental data available for comparison and calibration. An interesting alternative approach has been investigated by Gendron *et al*. [40, 41] that makes no direct reference to spin Hamiltonian parameters. The chemical shift is evaluated as a sum over states expression involving matrix elements of Zeeman and hyperfine operators over a set of spin-orbit states. The preliminary application of this approach shows much promise. However until such methods are more widely developed and implementations become more readily available, the spin Hamiltonian-based approach adopted in this work is likely to continue to provide the primary approach to studying heavy element PNMR shifts.

ACKNOWLEDGEMENTS

HMM thanks the Nuclear FiRST Doctoral Training Centre and the EPRSC for the award of a studentship during which this work was carried out. The authors also thank IT services (University of Manchester) for the provision of time on the RedQueen and Computational Shared Facilities.

CONFLICT OF INTEREST STATEMENT

The authors declare there are no conflicts of interest.

SUPPLEMENTARY INFORMATION

S1. Optimised geometries

Table S1.1. Comparison of key bond lengths between the crystal and optimised structures for molecules **1-18**.

Table S1.2. Comparison of key bond angles between the crystal and optimised structures for molecules **1-18**.

S2. Detailed results

Table S2.1.Active space selection for molecules **1-14**.

Table S2.2 to S2.18. Extended results for molecules **1-14** at varying levels of state averaging.

S1. Optimised geometries

Key distances (S1.1) and angles (S1.2) from structures optimised using the aZORA scheme are shown in comparison with crystal structure data.

Table S1.1. Comparison of key distances from the crystal structure data and optimised geometries of the molecules studied in this work.

Molecule	Distance	Crystal/Å	Optimised/Å	Ref.
1	Average U-Centroid Average U-C	1.99 2.53	1.95 2.55	[57]
2	Average U-N U-O Average U-C_{COT} U-$Centroid_{COT}$	2.12 2.47 2.68 1.96	2.12 2.46 2.67 1.92	[73]
4	Average U-N Average U-C_{Cp1} U-$Centroid_1$ Average U-C_{Cp2} U-$Centroid_2$	2.16 2.76 2.48 2.77 2.50	2.14 2.73 2.45 2.75 2.47	[74]
7	U = O U-N average N-Si	1.82 2.24 1.74	1.81 2.23 1.77	[76]
8	Average Ce-N_1 Average Ce-N_2 Average Ce-N_3	2.64 2.61 3.46	2.65 2.63 3.47	[77]
11	Average U-C Average U-CH_3 Average U-Centroid	2.85 3.93 2.58	2.79 3.91 2.52	[86]

Table S1.1. continued..

14	Average U-N Average U-Si	2.41 3.47	2.38 3.48	[71]
15	Average Th-CH_3 Average Th-C_{Cp} Th-$Centroid_{Cp}$	2.40 2.79 2.51	2.46 2.82 2.55	[51]
16	Average Th-Cl Average Th-C_{Cp} Th-$Centroid_{Cp}$	2.62 2.79 2.51	2.62 2.79 2.51	[51]
17	Th-Cl Average Th-C_{COT} Th-$Centroid_{COT}$ Average Th-C_{Cp} Th-$Centroid_{Cp}$	2.69 2.71 1.99 2.80 2.53	2.68 2.71 1.98 2.80 2.52	[52]
18	Th-Cl Average Th-Cp Average Th-$Centroid_{Cp}$	2.64 2.79 2.52	2.67 2.84 2.58	[53]

Table S1.2. Comparison of key angles from the crystal structure data and optimised geometries of the molecules studied in this work.

Molecule	**Angle**	**Crystal/°**	**Optimised/°**	**Ref.**
1	$Centroid_1$-U- $Centroid_2$	180.00	180.00	[57]
2	N_1-U-N_2	99.20	99.45	[73]
	O-U-Centroid	125.30	122.27	
	Average N-U-Centroid	125.37	124.43	
	Average O-U-N	84.30	87.76	
4	N_1-U-N_2	108.22	107.07	[74]
	$Centroid_1$-U-$Centroid_2$	132.59	129.5	
7	Average N-U-N	119.83	119.82	[76]
	Average O-U-N	92.39	92.48	
8	Average N-Ce-N	120.00	120.00	[77]
11	Average Centroid-U-Centroid	120.00	120.00	[86]
14	Average N-U-N	120.00	119.99	[71]
15	Cp-Th-Cp COT-Th-COT CH3-Th-CH3	143.83 100.87 96.20	148.41 104.46 91.10	[51]
16	Cp-Th-Cp COT-Th-COT Cl-Th-Cl	146.24 101.86 91.86	143.83 100.88 96.20	[51]
17	Cp-Th-COT Cp-Th-Cl COT-Th-Cl	140.49 98.84 120.67	140.01 99.54 120.44	[52]
18	Cp-Th-Cp Cp-Th-Cl	117.88 98.45	117.80 98.61	[53]

S2. Detailed results

This section reports extended results for the calculated PNMR chemical shifts for the molecules studied in this work. All shifts are given in ppm relative to tetramethylsilane. All calculations of ^{1}H NMR chemical shifts use an optimised geometry. ^{13}C and ^{29}Si results use either a crystal or optimised structure which is stated as appropriate. The optimised geometries were performed in Gaussian 09 using the aZORA scheme to provide a relativistic treatment alongside the exchange-correlation functional PBE0. The SARC basis set was employed on the heavy element, and Def2-SVP was used on all other nuclei.

The orbital shielding, $\sigma^{\mathrm{iso}}_{\mathrm{orb},K}$, was calculated using the GIAO method as implemented in Gaussian 09. The aZORA relativistic method and PBE0 functional were used. The SARC basis set was employed on the heavy element and Def2-TZVP on the nuclei of interest (with the exception of ^{13}C NMR of **11** where a decontracted Def2-SVP basis set was used on carbon). $\sigma^{\mathrm{iso}}_{K,\mathrm{Ref}}$ of the reference compound TMS was calculated using the same method and basis set as $\sigma^{\mathrm{iso}}_{\mathrm{orb},K}$.

The **g** tensor calculation was performed in ORCA 3.0.3 using the effective Hamiltonian approach as outlined in reference [67]. The active space chosen for each molecule is listed in Table S2.1. The SARC basis set was used on the heavy element. For molecules **1**-**6** Def2-TZVP was used on all light nuclei (see reference [35]). For molecules **7**-**14**, Def2-SVP was used on hydrogen nuclei and Def2-TZVP on all other light nuclei. The number of states included in the state averaging process was varied and the NMR chemical shift re-evaluated for comparison. The first column in Tables S2.2 to S2.18 details the number of states included. f^1 systems include doublet states and f^3 systems include quartet and doublet states. The detailed results for molecule **2** and **11** are reported in the main text (Tables 4 and 5 for **2** and Table 10 for **11**). Molecules **4**, **7** and **8** use a (1,7) active space with all 7 doublet states included. Therefore only one **g** tensor calculation was performed and the results are available in the main text (Table 8).

Table S2.1. Active space used in the **g** tensor calculation of molecules **1-14**. For a discussion on the choice of active space see reference [35].

Molecule	**Active space** *(electrons, orbitals)*
1	(5,9)
2	(5,9)
3	(5,9)
4	(1,7)
5	(5,9)
6	(1,7)/(5,9)
7	(1,7)
8	(1,7)
9	(3,7)
10	(3,7)
11	(3,7)
12	(3,7)
13	(3,7)
14	(3,7)

Table S2.2. Calculated ^{1}H chemical shifts for **1** using a fully uncontracted basis set for the **A** tensor calculation. Def2-TZVP was employed on C/H atoms with three additional steep s-type functions on H. The SARC basis was used on the uranium atom.

Number of doublet states averaged (g tensor)	δ_{H}^{iso} **(HFCC$_1$ for A tensor)**	δ_{H}^{iso} **(HFCC$_2$ for A tensor)**
Experimental [57]	*-38.7*	
5	-29.0	-22.8
7	-29.0	-22.7
9	-29.2	-22.9
11	-28.4	-22.2
15	-28.8	-22.5
21	-34.2	-27.1
31	-34.7	-27.4
41	-33.4	-26.4
61	-33.5	-26.5
101	-32.4	-25.6

Table S2.3. Calculated ^{1}H chemical shift of **3** using HFCC$_1$ for the **A** tensor calculation.

Number of doublet states averaged (g tensor)	δ_{H}^{iso} **(CH$_2$)**	δ_{H}^{iso} **(CH$_3$)**	δ_{H}^{iso} **(C$_8$H$_8$)**
Experimental [73]	*13.8*	*0.2*	*-9.5*
5	29.4	1.5	-19.7
7	31.4	1.3	-20.5
10	33.6	1.2	-22.2
20	35.8	1.3	-24.3
30	37.3	1.2	-25.3
40	37.0	1.4	-26.0
50	37.5	1.4	-26.7
60	37.4	1.4	-26.3
70	39.6	1.0	-26.1

Table S2.4. Calculated ^{1}H chemical shift of **3** using HFCC$_2$ for the **A** tensor calculation.

Number of doublet states averaged (g tensor)	δ_{H}^{iso} **(CH$_2$)**	δ_{H}^{iso} **(CH$_3$)**	δ_{H}^{iso} **(C$_8$H$_8$)**
Experimental [73]	*13.8*	*0.2*	*-9.5*
5	23.8	1.2	-16.3
7	25.6	1.1	-17.0
10	27.4	0.9	-18.5
20	29.1	1.0	-21.0

Table S2.4. continued..

30	30.5	0.9	-21.2
40	30.0	1.1	-21.8
50	30.4	1.1	-22.4
60	30.3	1.2	-22.4
70	32.5	0.7	-21.8

Table S2.5. Calculated ^{1}H chemical shift of **5** using $HFCC_1$ for the **A** tensor calculation.

Number of doublet states averaged (g tensor)	δ_H^{iso} **(C_8H_8)**	δ_H^{iso} **(CH_3)**	δ_H^{iso} **(C_5H_5)**	δ_H^{iso} **(CH_2)**
Experimental [73]	*-12.5*	*0.3*	*-3.2*	*22.5*
5	-27.8	0.1	-11.9	37.4
10	-31.0	-0.5	-10.6	38.2
20	-35.6	-0.6	-11.3	41.9
30	-37.2	-1.1	-11.2	42.6
40	-36.9	-1.0	-11.0	42.6
50	-37.8	-1.0	-11.2	43.4
60	-37.6	-0.9	-11.2	43.4

Table S2.6. Calculated ^{1}H chemical shift of **5** using $HFCC_2$ for the **A** tensor calculation.

Number of doublet states averaged (g tensor)	δ_H^{iso} **(C_8H_8)**	δ_H^{iso} **(CH_3)**	δ_H^{iso} **(C_5H_5)**	δ_H^{iso} **(CH_2)**
Experimental [73]	*-12.5*	*0.3*	*-3.2*	*22.5*
5	-21.7	-0.3	-9.8	27.1
10	-24.4	-0.9	-8.4	27.0
20	-28.1	-1.1	-8.9	29.3
30	-29.4	-1.6	-8.8	29.6
40	-29.2	-1.5	-8.6	29.7
50	-29.9	-1.5	-8.6	30.2
60	-29.7	-1.4	-8.7	30.2

Table S2.7. Calculated ^{1}H chemical shift of **6** using $HFCC_1$ for the **A** tensor calculation. (1,7) and (5,9) active spaces were both used to calculate the **g** tensor.

Number of doublet states averaged (g tensor)	δ_H^{iso} **(C_8H_8)**	δ_H^{iso} **(CH)**	δ_H^{iso} **(CH_3)**
Experimental [73]	*-6.6*	*14.8*	*1.8*
(1,7)			
7	-10.4	21.5	2.3
(5,9)			

Table S2.7. continued..

5	-13.4	23.4	3.0
7	-13.4	23.5	2.9
9	-14.8	24.8	3.1
10	-14.9	24.9	3.1
11	-14.9	24.9	3.1
13	-15.2	25.2	3.1
16	-16.7	26.6	3.2
19	-16.6	26.8	3.2
21	-17.2	27.2	3.2
23	-17.4	27.5	3.2
30	-18.7	28.6	3.4
50	-19.8	29.6	3.5

Table S2.8. Calculated ^{1}H chemical shift of **6** using $HFCC_2$ for the **A** tensor calculation. (1,7) and (5,9) active spaces were both used to calculate the **g** tensor.

Number of doublet states averaged (g tensor)	δ_H^{iso} **(C_8H_8)**	δ_H^{iso} **(CH)**	δ_H^{iso} **(CH_3)**
Experimental [73]	*-6.6*	*14.8*	*1.8*
(1,7)			
7	-8.2	19.2	2.1
(5,9)			
5	-11.0	20.8	2.8
7	-11.0	20.9	2.7
9	-12.2	22.1	2.9
10	-12.3	22.1	2.8
11	-12.3	22.2	2.8
13	-12.6	22.4	2.9
16	-13.8	23.6	3.0
19	-13.8	23.7	2.9
21	-14.3	24.1	3.0
23	-14.4	24.4	2.9
30	-15.6	25.3	3.1
50	-16.6	26.2	3.2

Table S2.9. Calculated ^{1}H chemical shift of **9** using $HFCC_1$ for the **A** tensor calculation.

Number of states averaged (g tensor)		δ_H^{iso} **(4-py)**	δ_H^{iso} **(3,5-py)**	δ_H^{iso} **(CH_3)**	δ_H^{iso} **(CH_3)**
Quartets	**Doublets**				
Experimental [77, 78]		*33.6*	*6.0*	*4.6*	*-17.5*
6		41.7	-12.6	15.1	-28.1
9		48.1	-8.4	12.4	-29.1
12		68.1	-11.1	13.8	-42.0

Table S2.9. continued..

13		60.4	-16.1	13.8	-40.2
13	**4**	48.5	-12.0	14.6	-31.3
13	**11**	67.5	-27.8	24.1	-50.8
14		60.0	-15.7	16.8	-39.8
14	**25**	67.5	-23.5	21.5	-48.4
21		58.6	-14.2	15.9	-38.2
30		56.0	-12.0	14.6	-35.5
35		52.8	-8.0	13.8	-33.0

Table S2.10. Calculated ^{1}H chemical shift of **9** using $HFCC_2$ for the **A** tensor calculation.

Number of states averaged (g tensor)		δ_H^{iso} **(4-py)**	δ_H^{iso} **(3,5-py)**	δ_H^{iso} **(CH_3)**	δ_H^{iso} **(CH_3)**
Quartets	**Doublets**				
Experimental [77, 78]		*33.6*	*6.0*	*4.6*	*-17.5*
6		26.4	-36.1	26.1	-34.3
9		48.5	-22.7	18.2	-37.2
12		83.4	-22.2	17.0	-54.4
13		56.9	-37.9	26.4	-50.8
13	**4**	42.0	-31.8	23.5	-39.2
13	**11**	45.7	-65.6	41.8	-62.1
14		56.7	-37.2	26.0	-50.2
14	**25**	55.2	-54.4	35.4	-60.1
21		57.2	-33.8	24.1	-48.4
30		56.6	-29.0	21.6	-45.3
35		51.7	-10.7	13.8	-33.3

Table S2.11. Calculated range of ^{1}H chemical shift of **10** (geometry 1) using $HFCC_1$ for the **A** tensor calculation.

Number of states averaged (g tensor)		δ_H^{iso} **range**	δ_H^{iso} **max-min**
Quartets	**Doublets**		
Experimental [82]		*12.4 to -0.2*	*12.6*
8		39.0 to -22.4	61.4
10		26.4 to -14.0	40.4
13		26.2 to -12.7	38.9
13	**11**	29.1 to -15.3	45.4
13	**20**	26.8 to -13.6	40.4
13	**35**	26.8 to -13.5	40.3
21		26.8 to -13.4	40.2
21	**40**	27.4 to -14.0	41.4

Table S2.11. continued..

22		26.7 to -13.3	40.0
22	**43**	27.1 to -13.8	40.9
30		26.2 to -12.7	38.9
35		26.0 to -12.4	38.4

Table S2.12. Calculated range of ^{1}H chemical shift of **10** (geometry 1) using $HFCC_2$ for the **A** tensor calculation.

Number of states averaged (g tensor)		δ_H^{iso} **range**	δ_H^{iso} **max-min**
Quartets	**Doublets**		
Experimental [82]		*12.4 to -0.2*	*12.6*
8		110.9 to -76.5	187.4
10		76.3 to -50.1	126.4
13		70.9 to -46.0	116.9
13	**11**	81.4 to -53.9	135.3
13	**20**	74.5 to -48.7	123.2
13	**35**	74.3 to -48.7	123.0
21		73.9 to -48.3	122.2
21	**40**	76.1 to -49.9	126.0
22		73.2 to -47.7	120.9
22	**43**	75.5 to -49.5	125.0
30		70.8 to -45.9	116.7
35		69.9 to -45.2	115.1

Table S2.13. Calculated range of ^{1}H chemical shift of **10** (geometry 2) using $HFCC_1$ for the **A** tensor calculation.

Number of states averaged (g tensor)		δ_H^{iso} **range**	δ_H^{iso} **max-min**
Quartets	**Doublets**		
Experimental [82]		*12.4 to -0.2*	*12.6*
10		13.3 to -9.5	22.8
13		15.1 to -4.7	19.8
13	**11**	16.3 to -3.3	19.6
13	**20**	16.6 to -2.1	18.7
13	**35**	16.6 to -2.1	18.7
21		15.0 to -5.6	20.6
21	**40**	16.5 to -2.6	19.1
22		15.0 to -5.6	20.6
22	**43**	16.6 to -2.3	18.9
30		15.1 to -5.1	20.2
35		15.1 to -5.0	20.1

Table S2.14. Calculated range of ^{1}H chemical shift of **10** (geometry 2) using $HFCC_2$ for the **A** tensor calculation.

Number of states averaged (g tensor)		δ_H^{iso} range	δ_H^{iso} max-min
Quartets	**Doublets**		
Experimental [82]		*12.4 to -0.2*	*12.6*
10		34.2 to -36.0	70.2
13		22.8 to -21.7	44.5
13	**11**	19.4 to -17.4	36.8
13	**20**	16.6 to -13.9	30.5
13	**35**	16.5 to -13.7	30.2
21		25.0 to -24.5	49.5
21	**40**	17.7 to -15.2	32.9
22		24.9 to -24.3	49.2
22	**43**	17.2 to -14.7	31.9
30		23.5 to -22.6	46.1
35		23.4 to -22.4	45.8

$HFCC_1$ and $HFCC_2$ methods yield very similar A_{FC} values; however the $\mathbf{A}_{SD}$ matrices produced are quite different giving a larger δ_{PC} term for the $HFCC_2$ calculations. This results in overestimated shifts for molecule **10** at both geometries when $HFCC_2$ is used. The influence of picture change effects on this molecule was checked and found to be negligible.

Table S2.15. Calculated ^{29}Si chemical shifts in **12** (crystal structure) using $HFCC_1$.

Number of states averaged (g tensor)		δ_{Si}^{iso}
Quartets	**Doublets**	
Experimental [87, 88]		*-155.0*
6		-154.8
13		-180.5
14		-180.2
14	**27**	-141.5
21		-178.8
21	**39**	-136.1
24		-178.6
24	**43**	-137.5
30		-178.3
30	**54**	-130.7
35		-177.8

Table S2.16. Calculated ^{29}Si chemical shifts in **13** (crystal structure) using $HFCC_1$.

Number of states averaged (g tensor)		δ_{Si}^{iso}
Quartets	**Doublets**	
Experimental [89]		*-136.7*
5		-136.1
9		-142.5
13		-151.3
13	**11**	-165.4
13	**24**	-173.1
13	**32**	-174.3
21		-151.1
21	**39**	-174.6
24		-150.8
24	**43**	-174.5
28		-150.6
28	**45**	-174.6
30		-150.5
30	**47**	-174.7
35		-150.3

Table S2.17. Calculated ^{29}Si chemical shift in **14** (crystal structure) using $HFCC_1$.

Number of states averaged (g tensor)		δ_{Si}^{iso}
Quartets	**Doublets**	
Experimental [71]		*-296.0*
6		-305.6
11		-331.6
13		-337.5
13	**11**	-361.4
13	**20**	-376.2
21		-336.6
21	**39**	-374.7
30		-336.5
35		-335.0

Table S2.18. Calculated ^{29}Si chemical shift in **14** (optimised structure) using $HFCC_1$.

Number of states averaged (g tensor)		δ_{Si}^{iso}
Quartets	**Doublets**	
Experimental [71]		*-296.0*
6		-266.3
11		-324.2
12		-322.3
13		-330.8
13	11	-290.8
14		-324.4
14	31	-312.2
21		-322.9
21	39	-314.6
22		-325.4
22	46	-318.3
30		-328.9
33		-316.8
35		-322.4

REFERENCES

1. Natrajan, L. S. and Paden, M. H. L. 2013, Element Recovery and Sustainability, A. Hunt, (Ed.), The Royal Society of Chemistry, Cambridge, 140.
2. Layfield, R. A. and Murugesu, M. 2015, Lanthanides and Actinides in Molecular Magnetism, Wiley-VCH, Weinheim.
3. Lucas, J., Lucas, P., Le Mercier, T., Rollat, A. and Davenport, W. 2015, Rare Earths Science, Technology, Production and Use, Elsevier B.V., Amsterdam, 231.
4. Rahman, A. and Choudhary, M. I. 2015, Applications of NMR Spectroscopy, Elsevier, Amsterdam.
5. Schreckenbach, G. and Ziegler, T. 1998, Theor. Chem. Acc., 99, 71.
6. Helgaker, B. T., Jaszunski, M. and Ruud, K. 1999, Chem. Rev., 99, 293.
7. Kaupp, M., Bühl, M. and Malkin, V. G. 2004, Calculation of NMR and EPR Parameters, Wiley-VCH, Weinheim.
8. Lodewyk, M. W., Siebert, M. R. and Tantillo, D. J. 2012, Chem. Rev., 112, 1839.
9. Grimblat, N. and Sarotti, A. M. 2016, Chem. Eur. J., 22, 12246.
10. Streitwieser Jr., A. and Yoshida, N. 1969, J. Am. Chem. Soc., 91, 7528.
11. Edelstein, N., Lamar, G. N., Mares, F. and Streitwieser Jr., A. 1971, Chem. Phys. Lett., 8, 399.
12. Adam, C., Kaden, P., Beele, B. B., Müllich, U., Trumm, S., Geist, A., Panak, P. J. and Denecke, M. A. 2013, Dalt. Trans., 42, 14068.
13. Adam, C., Beele, B. B., Geist, A., Müllich, U., Kaden, P. and Panak, P. J. 2015, Chem. Sci., 6, 1548.
14. Adam, C., Rohde, V., Müllich, U., Kaden, P., Geist, A., Panak, P. J. and Geckeis, H. 2016, Procedia Chem., 21, 38.
15. Vaara, J. 2013, High Resolution NMR Spectroscopy, R. H. Conteras, (Ed.), Elsevier, Amsterdam, 41.
16. Autschbach, J. 2015, Annu. Rep. Comput. Chem., 11, 3.
17. Rinkevicius, Z., Vaara, J., Telyatnyk, L. and Vahtras, O. 2003, J. Chem. Phys., 118, 2550.
18. Telyatnyk, L., Vaara, J., Rinkevicius, Z. and Vahtras, O. 2004, J. Phys. Chem. B, 108, 1197.
19. Pennanen, T. O. and Vaara, J. 2005, J. Chem. Phys., 123, 174102.
20. Rastrelli, F. and Bagno, A. 2009, Chem. Eur. J., 15, 7990
21. Aquino, F., Pritchard, B. and Autschbach, J. 2012, J. Chem. Theory Comput., 8, 598.
22. Hrobárik, P., Reviakine, R., Arbuznikov, A. V., Malkina, O. L., Malkin, V. G., Köhler, F. H. and Kaupp, M. 2007, J. Chem. Phys., 126, 1.
23. Rastrelli, F. and Bagno, A. 2010, Magn. Reson. Chem., 48, 132.
24. Rouf, S. A., Mareš, J. and Vaara, J. 2015, J. Chem. Theory Comput., 11, 1683.
25. Bühl, M., Ashbrook, S. E., Dawson, D. M., Doyle, R. A., Hrobárik, P., Kaupp, M. and Smellie, I. A. 2016, Chem. Eur. J., 22, 15328.
26. Autschbach, J., Patchkovskii, S. and Pritchard, B. 2011, J. Chem. Theory Comput., 7, 2175.
27. Martin, B. and Autschbach, J. 2015, J. Chem. Phys., 142, 54108.
28. Borgogno, A., Rastrelli, F. and Bagno, A. 2014, Dalt. Trans., 43, 9486.
29. Rudolph, R., Blom, B., Yao, S., Meier, F., Bill, E., Gastel, M. Van, Lindenmaier, N., Kaupp, M. and Driess, M. 2014, Organometallics, 33, 3154.
30. Mareš, J., Liimatainen, H., Pennanen, T. O. and Vaara, J. 2011, J. Chem. Theory Comput., 7, 3248.
31. Mareš, J., Hanni, M., Lantto, P., Lounila, J., Vaara, J. and Online, V. A. 2014, Phys. Chem. Chem. Phys., 16, 6916.
32. Borgogno, A., Rastrelli, F. and Bagno, A. 2015, Chem. Eur. J., 21, 12960.
33. Novotný, J., Sojka, M., Komorovsky, S., Nečas, M. and Marek, R. 2016, J. Am. Chem. Soc. 138, 8432.
34. Michael, D. 2015, Computational Methods in Lanthanide and Actinide Chemistry, John Wiley & Sons, Chicester.
35. Moylan, H. M. and McDouall, J. J. W. 2017, Chem. Eur. J., 23, 7798.
36. Autschbach, J. and Pritchard, B. 2011, Theor. Chem. Acc., 129, 453.
37. Rodríguez-Rodríguez, A., Esteban-Gómez, D., De Blas, A., Rodríguez-Blas, T., Fekete, M., Botta, M., Tripier, R. and Platas-Iglesias, C. 2012, Inorg. Chem., 51, 2509.

38. Rodríguez-Rodríguez, A., Esteban-Gómez, D., De Blas, A., Rodríguez-Blas, T., Botta, M., Tripier, R. and Platas-Iglesias, C. 2012, Inorg. Chem., 51, 13419.
39. Fusaro, L., Casella, G. and Bagno, A. 2015, Chem. Eur. J., 21, 1955.
40. Gendron, F., Sharkas, K. and Autschbach, J. 2015, J. Chem. Phys. Lett., 6, 2183.
41. Gendron, F. and Autschbach, J. 2016, J. Chem. Theory Comput., 12, 5309.
42. Soncini, A. and van Den Heuvel, W. 2013, J. Chem. Phys., 138, 21103.
43. Vaara, J., Rouf, S. A. and Mares, J. 2015, J. Chem. Theory Comput., 11, 4840.
44. Gaussian 09, Revision B.01, Frisch, M. J., Trucks, G. W., Schlegel, H. B., Scuseria, G. E., Robb, M. A., Cheeseman, J. R., Scalmani, G., Barone, V., Mennucci, B., Petersson, G. A., Nakatsuji, H., Caricato, M., Li, X., Hratchian, H. P., Izmaylov, A. F., Bloino, J., Zheng, G., Sonnenberg, J. L., Hada, M., Ehara, M., Toyota, K., Fukuda, R., Hasegawa, J., Ishida, M., Nakajima, T., Honda, Y., Kitao, O., Nakai, H., Vreven, T., Montgomery, J. A., Jr., Peralta, J. E., Ogliaro, F., Bearpark, M., Heyd, J. J., Brothers, E., Kudin, K. N., Staroverov, V. N., Kobayashi, R., Normand, J., Raghavachari, K., Rendell, A., Burant, J. C., Iyengar, S. S., Tomasi, J., Cossi, M., Rega, N., Millam, J. M., Klene, M., Knox, J. E., Cross, J. B., Bakken, V., Adamo, C., Jaramillo, J., Gomperts, R., Stratmann, R. E., Yazyev, O., Austin, A. J., Cammi, R., Pomelli, C., Ochterski, J. W., Martin, R. L., Morokuma, K., Zakrzewski, V. G., Voth, G. A., Salvador, P., Dannenberg, J. J., Dapprich, S., Daniels, A. D., Farkas, Ö., Foresman, J. B., Ortiz, J. V., Cioslowski, J., Fox, D. J. 2009, Gaussian, Inc., Wallingford CT.
45. van Lenthe, J. H., Faas, S. and Snijders, J. G. 2000, Chem. Phys. Lett., 328, 107.
46. Filatov, M. 2002, Chem. Phys. Lett., 365, 222.
47. Pantazis, D. A. and Neese, F. 2009, J. Chem. Theory Comput., 5, 2229.
48. Pantazis, D. A. and Neese, F. 2011, J. Chem. Theory Comput., 7, 677.
49. Weigend, F. and Ahlrichs, R. 2005, Phys. Chem. Chem. Phys., 7, 3297.
50. Adamo, C. and Barone, V. 1999, J. Chem. Phys., 110, 6158.
51. Trnka, T. M., Bonanno, J. B., Bridgewater, B. M. and Parkin, G. 2001, Organometallics, 20, 3255.
52. Button, Z. E., Higgins, J. A., Suvova, M., Cloke, F. G. N. and Roe, S. M. 2015, Dalton Trans., 44(6), 2588-2596.
53. Cloke, F. G. N., Hawkes, S. A., Hitchcock, P. B. and Scott, P. 1994, Organometallics, 13, 2895.
54. Ditchfield, R. 1974, Mol. Phys., 27, 789.
55. Wolinski, K., Hinton, J. F. and Pulay, P. 1990, J. Am. Chem. Soc., 112, 8251.
56. Autschbach, J. 2013, High Resolution NMR Spectroscopy, R. H. Contreras, (Ed.), Elsevier, Amsterdam, 69.
57. Arliguie, T., Lance, M., Nierlich, M., Vigner, J. and Ephritikhine, M. 1995, J. Chem. Soc., Chem. Commun., 44 , 183.
58. Gourier, D., Caurant, D., Arliguie, T. and Ephritikhine, M. 1998, J. Am. Chem. Soc., 120, 6084.
59. Chipman, D. M. 1992, Theor. Chim. Acta, 82, 93.
60. Barone, V. 1996, Recent Advances in Density Functional Methods Part I, D. Chong, (Ed.), World Scientific Publishing Company, Singapore, 287.
61. Kutzelnigg, W., Fleischer, U. and Schindler, M. 1991, NMR Basic Principles and Progress, Springer Verlag, Berlin/Heidelberg, 165.
62. Jensen, F. 2006, J. Chem. Theory Comput., 2, 1360.
63. Neese, F. 2012, Wiley Interdiscip. Rev. Comput. Mol. Sci., 2, 73.
64. Hess, B. A. 1985, Phys. Rev. A, 32, 756.
65. Jansen, G. and Hess, B. A. 1989, Phys. Rev. A, 39, 6016.
66. Sandhoefer, B. and Neese, F. 2012, J. Chem. Phys., 137, 94102.
67. Atanasov, M., Aravena, D., Suturina, E., Bill, E., Maganas, D. and Neese, F. 2015, Coord. Chem. Rev., 289, 177.
68. Neese, F. 2005, J. Chem. Phys., 122, 34107.
69. Luzanov, A. V., Babich, E. N. and Ivanov, V. V. 1994, J. Mol. Struct., 311, 211.
70. Bolvin, H. 2006, ChemPhysChem, 7, 1575.
71. Goodwin, C. A. P., Tuna, F., McInnes, E. J. L., Liddle, S. T., McMaster, J., Vitorica-Yrezabal, I. J. and Mills, D. P. 2014, Chem. Eur. J., 20, 14579.

72. Chibotaru, L. F. and Ungur, L. 2012, J. Chem. Phys., 137, 64112.
73. Boisson, C., Berthet, J. C., Lance, M., Vigner, J., Nierlich, M. and Ephritikhine, M. 1996, J. Chem. Soc. Dalt. Trans., 947.
74. Boisson, C., Berthet, J. C., Lance, M., Nierlich, M., Vigner, J. and Ephritikhine, M. 1995, J. Chem. Soc. Chem. Commun., 25, 543.
75. Andersen, R. A. 1979, Inorg. Chem., 18, 1507.
76. Fortier, S., Brown, J. L., Kaltsoyannis, N., Wu, G. and Hayton, T. W. 2012, Inorg. Chem., 51, 1625.
77. Iveson, P. B., Rivière, C., Guillaneux, D., Nierlich, M., Thuéry, P., Ephritikhine, M. and Madic, C. 2001, Chem. Commun., 1512
78. Berthet, J. C., Miquel, Y., Iveson, P. B., Nierlich, M., Thuéry, P., Madic, C. and Ephritikhine, M. 2002, J. Chem. Soc., Dalt. Trans., 2, 3265.
79. Kaltsoyannis, N. and Kerridge, A. 2014, The Chemical Bond: Chemical Bonding Across the Periodic Table, G. Frenking, and S. Sason, (Eds.), Wiley-VCH Verlag GmbH & Co. KGaA, Weinheim, 337.
80. Formanuik, A., Ariciu, A., Ortu, F., Beekmeyer, R., Kerridge, A., Tuna, F., Mcinnes, E. J. L. and Mills, D. P. 2017, Nat. Chem., 9, 578.
81. Cotton, S. 2006, Lanthanide and Actinide Chemistry, John Wiley & Sons, Chicester
82. Natrajan, L. S., Khoabane, N. M., Dadds, B. L., Muryn, C. A., Pritchard, R. G., Heath, S. L., Kenwright, A. M., Kuprov, I. and Faulkner, S. 2010, Inorg. Chem., 49, 7700.
83. Miertuš, S., Scrocco, E. and Tomasi, J. 1981, Chem. Phys., 55, 117.
84. Miertuš, S. and Tomasi, J. 1982, Chem. Phys., 65, 239.
85. Pascual-Ahuir, J. L., Silla, E. and Tuñon, I. 1994, J. Comput. Chem., 15, 1127.
86. Evans, W. J., Forrestal, K. J. and Ziller, J. W. 1997, Angew. Chem. Int. Ed. Engl., 36, 774.
87. Siladke, N. A., Ziller, J. W. and Evans, W. J. 2010, Z. Anorg. Allg. Chem., 636, 2347.
88. Windorff, C. J. and Evans, W. J. 2014, Organometallics, 33, 3786.
89. Tsoureas, N., Summerscales, O. T., Cloke, G. N. and Roe, S. M. 2013, Organometallics, 32, 1353.
90. Angeli, C., Cimiraglia, R., Evangelisti, S., Leininger, T. and Malrieu, J. P. 2001, J. Chem. Phys., 114, 10252.
91. Angeli, C., Cimiraglia, R. and Malrieu, J. P. 2001, Chem. Phys. Lett., 350, 297.
92. Angeli, C., Cimiraglia, R. and Malrieu, J. P. 2002, J. Chem. Phys., 117, 9138.

.